

The Symbiotic X-ray binaries Sct X-1, 4U 1700+24 and IGR J17329-2731

E. Bozzo,^{1,2*} P. Romano,³ C. Ferrigno,¹ and L. Oskinova,⁴

¹Department of Astronomy, University of Geneva, Chemin d'Ecogia 16, CH-1290 Versoix, Switzerland

²INAF-OAR, Via Frascati, 33, 00078 Monte Porzio Catone, Rome, Italy

³INAF, Osservatorio Astronomico di Brera, Via E. Bianchi 46, I-23807, Merate, Italy

⁴Institut für Physik und Astronomie, Universität Potsdam, Karl-Liebknecht-Strasse 24/25, 14476 Potsdam, Germany

ABSTRACT

Symbiotic X-ray binaries are systems hosting a neutron star accreting from the wind of a late type companion. These are rare objects and so far only a handful of them are known. One of the most puzzling aspects of the symbiotic X-ray binaries is the possibility that they contain strongly magnetized neutron stars. These are expected to be evolutionary much younger compared to their evolved companions and could thus be formed through the (yet poorly known) accretion induced collapse of a white dwarf. In this paper, we perform a broad-band X-ray and soft γ -ray spectroscopy of two known symbiotic binaries, Sct X-1 and 4U 1700+24, looking for the presence of cyclotron scattering features that could confirm the presence of strongly magnetized NSs. We exploited available *Chandra*, *Swift*, and *NuSTAR* data. We find no evidence of cyclotron resonant scattering features (CRSFs) in the case of Sct X-1 but in the case of 4U 1700+24 we suggest the presence of a possible CRSF at ~ 16 keV and its first harmonic at ~ 31 keV, although we could not exclude alternative spectral models for the broad-band fit. If confirmed by future observations, 4U 1700+24 could be the second symbiotic X-ray binary with a highly magnetized accretor. We also report about our long-term monitoring of the last discovered symbiotic X-ray binary IGR J17329-2731 performed with *Swift*/XRT. The monitoring revealed that, as predicted, in 2017 this object became a persistent and variable source, showing X-ray flares lasting for a few days and intriguing obscuration events that are interpreted in the context of clumpy wind accretion.

Key words: accretion: accretion discs; X-rays: stars; X-rays: binaries; stars: neutron; stars: massive; X-rays: individual: Sct X-1; X-rays: individual: 4U 1700+24; X-rays: individual: IGR J17329-2731.

1 INTRODUCTION

Symbiotic X-ray binaries (SyXBs) are rare low mass X-ray binaries (LMXBs) hosting a red giant and (in most cases) a neutron star (NS) accreting from the slow wind of its companion. Only five¹ SyXBs are known so far (Masetti et al. 2006, 2007b,a; Nucita et al. 2007; Corbet et al. 2008; Nespoli et al. 2008; Bozzo et al. 2013, 2018).

Although these sources are formally part of the LMXBs class due to the low mass of the red giant donor star, their behaviour in the X-ray domain strongly resembles that of the high mass X-ray binaries (HMXBs). SyXBs show long pulse periods, ranging from hundred of seconds to hours, and display a high pulsed fraction that can be as large as 30-50%. They are characterized by the longest orbital periods among the known LMXBs (several tens to thousand days) and a prominent variability in the X-ray domain by a factor of ~ 10 -20 typical of wind-fed HMXBs. These properties strongly suggest the presence of a highly magnetized NS (at least $>10^{12}$ G) in the SyXBs.

The evolutionary calculations available so far (Postnov et al. 2010; Lü et al. 2012; Kuranov & Postnov 2015) assume *a priori*

that the progenitor of a SyXB is a binary system initially hosting a strongly magnetized NS and a low mass main sequence star ($\lesssim 2 M_{\odot}$) in a wide orbit (hundreds of days). In the early stages of evolution, the secondary star is on the first giant branch but does not fill its Roche lobe, leading to a negligible mass transfer toward the NS and thus to negligible high-energy emission. When this is no longer the case, as the magnetic field of the NS is assumed not to have decayed and its rotational velocity is still high, the system enters in a so-called “propeller” phase. Inflowing material from the donor star is ejected from the vicinity of the NS and accretion is still largely inhibited. This occurs at the expense of the rotational energy, inducing a rapid increase of the NS spin period up to $\gtrsim 10\,000$ s (Bozzo et al. 2008; Shakura et al. 2012). As little to no accretion is taking place in this stage, the system is hardly detectable in the X-ray domain. The situation changes when the NS has slowed down sufficiently to reduce the centrifugal force at the magnetospheric boundary and allows some accretion to take place, finally shining as a SyXB. In this phase, accretion is still likely to take place directly from the stellar wind. As this is endowed with little to no angular momentum, the spin period of the NS is still expected to increase because of the effect of the friction between the relatively large magnetosphere and the surrounding dense environment. In the following evolutionary phase, the velocity of the stellar wind decreases to a level at which the formation of an accretion disk around the compact object is inevitable (Wang 1981). Accretion in this phase leads to rapid decrease

* E-mail: enrico.bozzo@unige.ch

¹ We take into account here the fact that 3A 1954+319 has been recently reclassified as a classical supergiant X-ray binary (Hinkle et al. 2020; Bozzo et al. 2022).

of the NS spin period and the system finally resembles a common LMXB with a fast spinning compact object (see Fig. 1 of Lü et al. 2012).

One of the most puzzling aspects of SyXBs concerns the presence of a strongly magnetized NS in a system that has to be at least several Gyr old to allow the donor star to evolve to the red giant phase. The measurement of the NS magnetic field is usually obtained through the detection of cyclotron resonant scattering features (CRSFs). These are absorption features in the X-ray spectra of NS binaries that were first discovered in Her X-1 (Trümper et al. 1977; Truemper et al. 1978) and later identified in several other systems (Heindl et al. 2004; Schönherr et al. 2007). Long-standing theoretical developments have shown that the NS magnetic field should decay with time especially in the presence of accretion, and this is the main reason why the bulk of the LMXBs host weakly magnetized NSs (Tauris 2015). An alternative possibility put forward is that the NS formed much later in the evolution of the SyXB due to the accretion induced collapse of a white dwarf accreting from the stellar wind of the red giant. The white dwarf would have an age compatible with that of the red giant companion, while the NS forms more recently after a long phase of accretion. This allows the NS to preserve its high magnetic field up to the point in time at which the system shines as a SyXB. So far, the accretion induced collapse of a white dwarf remains a relatively poorly known process and it is a matter of debate if a strongly magnetized NS (at the level of $\geq 10^{12}$ G) can be produced by conservation of a sufficiently intense white dwarf magnetic flux during the collapse (see, e.g., Tauris 2015, and references therein).

Only in the case of the SyXB IGR J17329–2731 the presence of a strongly magnetized NS could be firmly established thanks to the detection of a CRSF at ~ 21 keV, providing an estimate of the compact magnetic field strength as high as 2.4×10^{12} G (Bozzo et al. 2018). This discovery called for further observations of IGR J17329–2731, as well as of other SyXBs, to consolidate our understanding on the formation channels of these systems.

In this paper, we pursue the search for CRSFs in SyXBs through the broad-band spectral analysis of the X-ray emission from two known sources in this class, Sct X–1 and 4U 1700+24. For the first source, we report on our simultaneous observation with *Chandra* and *NuSTAR*. For 4U 1700+24, we exploit a public but yet unpublished *NuSTAR* observation, as well as previously performed broad-band observations with the XRT and BAT on-board *Swift* during three outbursts of the source that occurred in 2014 and 2015. We additionally report in this paper on the outcomes of our long-term observational campaign with *Swift*/XRT on the most recently discovered SyXB IGR J17329–2731, covering up to nine months after its first detection in the X-rays (August 2017).

2 Sct X–1

Sct X–1 was discovered in 1974 (Hill et al. 1974) and subsequently observed with a variety of X-ray facilities. The system is known to host a 111 s spinning NS and is characterized by a remarkably high local absorption column density reaching up to $\sim 10^{23}$ cm $^{-2}$. It also showed a prominent variability (from < 0.3 to 20 mCrab, corresponding to 5×10^{-12} to 3×10^{-10} erg cm 2 s $^{-1}$) on a large range of timescales and the presence of a neutral iron line emission that was detected in its X-ray spectrum already back in the '90s (the *HEAO 1* satellite detected Sct X–1 up to ~ 100 keV; see Koyama et al. 1991a, and references therein). The best determined source position to date was obtained through an *XMM-Newton* observation reported by

Kaplan et al. (2007). These authors could use the improved source localization (1 arcsec) to identify the optical counter-part of the X-ray source and proposed that the NS in Sct X–1 is coupled to a late type giant about 4 kpc away from us. This led to the classification of Sct X–1 as a SyXB in our Galaxy. The *XMM-Newton* data revealed also that the source had continuously spun down from the late '90s to 2004, and the best measured pulse period from *XMM-Newton* was 112.86 ± 0.08 s. Kaplan et al. (2007) further found that since the late '90s the source had decreased in flux substantially, reaching at the time of the *XMM-Newton* observation a flux of 0.4 Crab (corresponding to 1.2×10^{-11} erg cm 2 s $^{-1}$ in the 0.5–10 keV energy band). The spectrum measured by the EPIC cameras on-board *XMM-Newton* proved to be significantly harder compared to previous measures with *HEAO 1* and *Ginga* (the power-law photon index decreased from ~ 2.0 to ~ 1.5), and the absorption column density was shown to have decreased by a factor of few (from $2\text{--}4 \times 10^{23}$ cm $^{-2}$ to 8×10^{22} cm $^{-2}$; see Cooke et al. 1984; Koyama et al. 1991b). No additional X-ray observations were performed toward Sct X–1 between 2004 and 2014. More recently, De et al. (2022) reported on the first broad-band IR spectroscopic investigation of the source and re-classified the companion as a M8-9 III type O-rich Mira donor star, rather than a red giant. This makes Sct X–1 a peculiar member of the SyXBs and the first known NS binary with a Mira companion.

In this paper, we report on an observational campaign aimed at Sct X–1 (almost) simultaneously with *Chandra* and *NuSTAR*. We also exploit two yet unpublished archival *Suzaku* observations pointed at the source.

Sct X–1 was observed with *Chandra* on 2020 November 9 at 01:50 (UT) for a total exposure time of 28.7 ks (PI: E. Bozzo). The observation was carried out with the ACIS-S in Faint mode (timed exposure). We processed the *Chandra* data with standard techniques² using CIAO v4.3 and the latest CALDB available at the moment of writing (v.0460; released on 2021 September 23). Only one source was detected in the ACIS image extracted in the 0.5–10 keV and the best determined position using the CIAO (v4.3) tool CELLETECT is at RA=278.85755 and DEC= -7.61408 with an associated uncertainty at 90% c.l. of 0.6 arcsec. This position is fully consistent with that previously reported by Kaplan et al. (2007); De et al. (2022) and within 0.3 arcsec from the selected counterpart of Sct X–1 (2MASS J18352582–0736501). This confirms the classification of Sct X–1 with the Galactic SyXB.

Using the CIAO tool DMEXTRACT, we determined that only about 170 effective counts were recorded from the source and thus we did not attempt any timing investigation, limiting the analysis to the sole extraction of a time-averaged spectrum (rebinned to have at least 25 counts per energy bin). The corrected source spectrum was extracted using the CIAO tool SPECXTRACT and could be well fit ($\chi^2/\text{d.o.f.} = 6.1/7$) with a simple absorbed powerlaw model (TBABS*POW in XSPEC). We adopted the *wilm* abundances (Wilms et al. 2000) and *vern* cross sections (Verner et al. 1996). We measured an absorption column density of $N_{\text{H}} = (5.0_{-1.8}^{+2.5}) \times 10^{22}$ cm $^{-2}$ and a photon index of $\Gamma = 1.8_{-0.7}^{+0.9}$. The estimated 0.5–10 keV X-ray flux was 2.1×10^{-13} erg cm $^{-2}$ s $^{-1}$. These results are fully consistent with those reported by De et al. (2022).

NuSTAR observed Sct X–1 starting on 2020 November 8 at 18:16 for a total exposure time of 32.5 ks (PI: E. Bozzo). We reduced the data-set using standard techniques³ and the caldb version re-

² See <https://cxc.cfa.harvard.edu/ciao/threads>.

³ See https://heasarc.gsfc.nasa.gov/docs/nustar/analysis/nustar_swguide.pdf

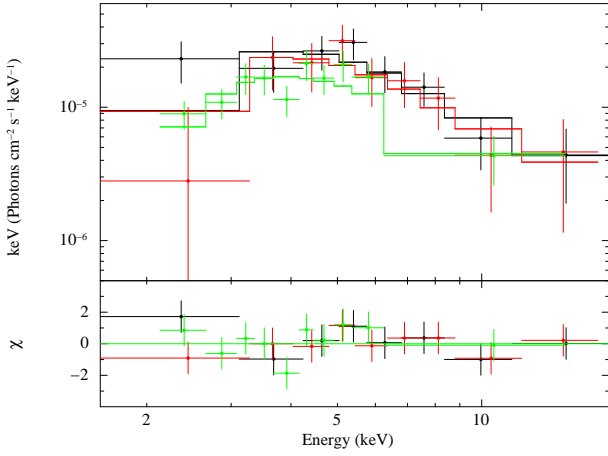


Figure 1. Broad-band (unfolded) X-ray spectrum of Sct X-1 combining the *Chandra* ACIS-S (green) with the *NuSTAR* FPMA (black) and FPMB (red) data. The best fit is obtained with a model comprising an absorbed powerlaw. The residuals from the fit are shown in the bottom panel.

leased in 2021 December 2. We first extracted both the FPMA and FPMB images and noted that a single faint source was detected at a location compatible with the *Chandra* position of Sct X-1 reported above. Given the faintness of the source (about 320 counts were collected by both the FPMs), it was not possible to carry out a study of the source lightcurve or perform any timing analysis. We thus extracted only the time averaged spectra (rebinned to have at least 25 counts per energy bin) and fit the data from both FPMs together. The source spectrum could be well described by an absorbed powerlaw model ($\chi^2/\text{d.o.f.} = 9.0/13$). We measured $N_{\text{H}} = (14.2^{+16.3}_{-10.8}) \times 10^{22} \text{ cm}^{-2}$ and $\Gamma = 3.8^{+1.2}_{-0.9}$. The estimated 3–20 keV X-ray flux was $2.5 \times 10^{-13} \text{ erg cm}^{-2} \text{ s}^{-1}$. A normalization constant was included in the fit to take into account cross-calibrations between the FPMA and FPMB but it turned out to be fully compatible with unity.

We also fit simultaneously the *Chandra* and *NuSTAR* data. In this case, we obtained $N_{\text{H}} = (8.6^{+3.8}_{-3.0}) \times 10^{22} \text{ cm}^{-2}$ and $\Gamma = 2.9^{+0.6}_{-0.5}$ ($\chi^2/\text{d.o.f.} = 17.7/22$). The normalization constant introduced to take into account cross-calibrations between *Chandra* and *NuSTAR* was measured at 0.6 ± 0.2 (fixing the *NuSTAR* constant to unity for reference). We show the results of the fit to the broad-band spectrum of Sct X-1 in Fig. 1.

We noted that two *Suzaku* observations of Sct X-1 were also carried out in 2014 October 10 at 12:43 and in 2014 October 22 at 02:45 (UT). The exposure time available for the XIS instrument was of 15.2 ks and 38.6 ks, respectively. We obtained from the HEASARC archive the pre-processed XIS data and verified that no source was detected at a position consistent with Sct X-1. We adopted the XIMAGE tool and the command UPLIMIT available within HEASOFT v.6.29c to estimate an upper limit on the source X-ray flux (see Bozzo et al. 2012, and references therein). From the shorter observation, we obtained a 3σ upper limit on the source count-rate of 0.22 cts s^{-1} , while the longer observation returned an upper limit of 0.15 cts s^{-1} . By using the online tool WEBPIMMS⁴ and the spectral model measured from the *Chandra* + *NuSTAR* data, we converted the above values into a 3σ upper limit on the source 0.5–10 keV X-ray flux of $8.6 \times 10^{-13} \text{ erg cm}^{-2} \text{ s}^{-1}$ and $5.6 \times 10^{-13} \text{ erg cm}^{-2} \text{ s}^{-1}$, respectively.

3 4U 1700+24

4U 1700+24 was discovered in the '70s and it is known since then to be a relatively bright persistent X-ray source (see, e.g., Garcia et al. 1983; Nucita et al. 2014; Hinkle et al. 2019, and references therein). The source is known to host an accreting NS which pulsations have been so far elusive most likely due to the pole-on direction through which the system is being observed. The source shows a remarkable variability in X-rays, achieving a total dynamic range of at least ~ 200 , considering also that the source has been detected undergoing short outbursts a few times by both *Swift* and *MAXI* (Kennea et al. 2014; Fukushima et al. 2014; Burrows et al. 2014, 2015). The M giant companion is relatively well studied and it has been recently reported though long-term optical and near-IR observations the discovery of its pulsating period (about 420 days), as well as the orbital period of the system measured at ~ 12.0 years (Hinkle et al. 2019). This is by far the longest known orbital period for a SyXB and the detailed modeling of the optical data provided support in favor of the previous finding that the system is observed pole-on, with an estimated orbital inclination of $11.3 \pm 0.4^\circ$. The measurement of the distance to the source has been also recently improved thanks to the Gaia data at $0.536 \pm 0.009 \text{ kpc}$ (Arnason et al. 2021).

In the soft X-ray domain ($\leq 10 \text{ keV}$), the spectral energy distribution of the source is usually described by using a model comprising a thermal black-body emission dominating below $\sim 2 \text{ keV}$ and a comptonization component (see, e.g., Nucita et al. 2014, and references therein). A red-shifted O VIII Ly- α transition line has been detected multiple times by using the RGSs on-board *XMM-Newton* and so far ascribed to either the re-organization of the X-ray emitting material close to the NS magnetic poles or to the presence of a uni-polar jet of matter emitted by the NS with velocities of the order of few 1000 km s^{-1} . A study of the broad-band X-ray emission from 4U 1700+24 was carried out in the past by Masetti et al. (2002) using a combination of *ROSAT*, *ASCA*, *RXTE*, and *BeppoSAX* data, as well as by Nagae et al. (2008) using *Suzaku* data. No evidence of a cyclotron line was found, with the broad-band spectra of the source being well described by the same combination of components mentioned above.

In this paper, we report on a yet unpublished *NuSTAR* observation of 4U 1700+24 carried out from 2014 October 2 at 10:26 (UT) to October 3 at 15:21 for a net exposure time of 51.6 ks over 102 ks of observation. We made use of data from both the FPMA and FPMB in the energy range 3–79 keV, processing the data with the `nupipeline` (version 0.4.9) available within the HEASOFT (version 6.29) and the version 20211020 of the calibration database. The processing provided us the cleaned event files. We used extraction regions of two arcminutes radius for both source and background products. These region files were used as input to `nuproducts` (version 0.3.3) to obtain the source and background lightcurves and spectra. We verified that different reasonable choices of the location of the background region and of the radius of extraction do not affect our results.

The source lightcurve was extracted with bins of one second and adaptively rebinned to reach a signal to noise ratio of at least 25 in each bin (see Bozzo et al. 2013, for details on the adaptive hardness ratio rebinning employed in several of our papers). As it can be appreciated in Fig. 2, the source lightcurve shows a moderate variability that is not accompanied by significant changes in the spectral properties (the hardness ratio, HR, remained virtually constant across the entire observation). This was confirmed by the usage of a Bayesian block analysis (the same exploited in a number of our previous papers; see, e.g., Ferrigno et al. 2020) which thus convinced

⁴ <https://heasarc.gsfc.nasa.gov/cgi-bin/Tools/w3pimms/w3pimms.pl>

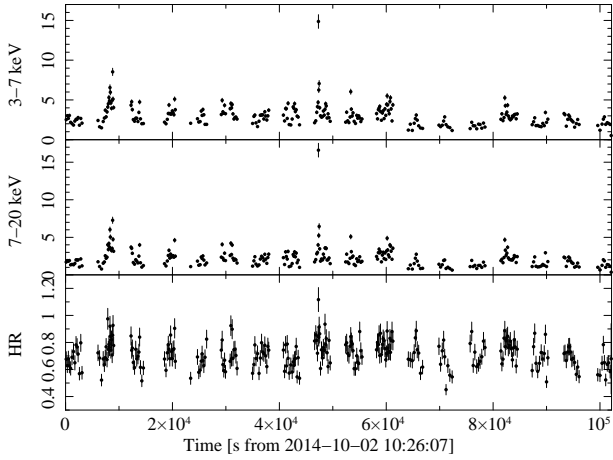


Figure 2. From top to bottom *NuSTAR* soft (3–7 keV), hard (7–20 keV) lightcurves of 4U 1700+24 and their ratio (HR).

us to extract a single spectrum using the entire exposure time available to investigate the properties of the broad-band X-ray emission from 4U 1700+24.

The spectrum in the 3–70 keV range was rebinned using the optimal grouping method described by [Kaastra & Bleeker \(2016\)](#) and the Cash statistics (C-stat in XSPEC) was adopted to evaluate the goodness of all fits. We first tested a simple phenomenological model to describe the source spectrum, comprising a cut-off power-law component ((`highcut*pegpwlw`) in XSPEC) attenuated by neutral absorption at the lower energies ((`TBabs`) in XSPEC). We adopted for the absorption component Vermmer cross sections ([Verner & Yakovlev 1995](#)) and “Wilm” abundances ([Wilms et al. 2000](#)). The best-fit parameters were determined using the modified Levenberg-Marquardt algorithm based on the CURFIT routine from Bevington, while uncertainties on the parameters were obtained by running a Monte Carlo Markov Chain (MCMC) with the Goodman-Weare sampling algorithm. We used 60 walkers, a burn-out of 6000 steps, and a chain length of 36 000. Priors were uniform for the slope and uniform in logarithmic scale for all other parameters. We set parameter limits wide enough not to influence the posteriors. To assess the goodness of the fit, we sampled 1 000 parameter sets derived from the MCMC, simulated a spectrum based on that model with the same exposure and background of the measured one, and performed a fit. We compared the C-stat of the simulated set to the one derived from the data and found that all simulations yield a better fit statistic. We thus concluded that the model had a probability less than 0.1% to be statistically acceptable.

Driven by the visual inspection of the residuals from the above fit, we tested the improvement of the results by adding to the simple phenomenological model either a black-body or two broad Gaussian absorption lines with centroid energies fixed to be one the double of the other. These two more complete models gave equivalently acceptable results. The black-body radius turned out in the fit to have a radius compatible with that of an hot spot on the NS surface, providing a 17% contribution to the total 1–10 keV unabsorbed flux. In the model featuring absorption Gaussian lines, the width of the fundamental feature is of 8 or 5 keV depending if we include or not the first harmonic in the fit. The latter turned out to be only marginally significant, but the different panels reported in Fig 3 shows how the introduction of this second feature is able to treat the otherwise evident residuals around 30 keV. All results of the above fits are summarized in Table 3. For completeness, we also tested alternative models

Table 1. Spectral fit results for the average *NuSTAR* spectrum of 4U 1700+24. Uncertainties are at 68% confidence level derived from the 16 and 84% quantiles of the MCMC.

Tbabs*highcut*(pegpwlw+bbbodyrad)		
N_{H}	1.8 ± 0.6	10^{22}cm^{-2}
E_{C}	$10.7^{+0.6}_{-0.8}$	keV
E_{F}	49^{+7}_{-6}	keV
T_{bb}	1.43 ± 0.03	keV
r	0.86 ± 0.08	km/10 kpc
Γ	1.96 ± 0.05	
Flux (1–10 keV) ^a	167 ± 13	$10^{-12} \text{erg s}^{-1} \text{cm}^{-2}$
Simulated fraction ^b	23%	
TBabs*gabs*highcut*pegpwlw		
N_{H}	$4.3^{+0.4}_{-0.3}$	10^{22}cm^{-2}
E_{Cyc1}	$16.4^{+0.7}_{-0.5}$	keV
σ_{Cyc1}	$5.1^{+1.4}_{-0.7}$	
τ_{Cyc1}	$1.7^{+1.0}_{-0.4}$	
E_{C}	7.5 ± 0.4	keV
E_{F}	43 ± 4	keV
Γ	2.07 ± 0.04	
Flux (1–10 keV)	248^{+8}_{-5}	$10^{-12} \text{erg s}^{-1} \text{cm}^{-2}$
Simulated fraction ^b	27%	
TBabs*gabs*gabs*highcut*pegpwlw		
N_{H}	$4.2^{+0.3}_{-0.5}$	10^{22}cm^{-2}
E_{Cyc1}^c	$16.0^{+0.6}_{-0.4}$	keV
σ_{Cyc1}	8 ± 1	keV
τ_{Cyc1}	5^{+2}_{-2}	
σ_{Cyc2}	$1.6^{+1.7}_{-0.9}$	keV
τ_{Cyc2}	$0.4^{+0.5}_{-0.3}$	
E_{C}	7.6 ± 0.4	keV
E_{F}	35 ± 4	keV
Γ	$2.01^{+0.04}_{-0.05}$	
Flux (1–10 keV)	259^{+13}_{-10}	$10^{-12} \text{erg s}^{-1} \text{cm}^{-2}$
Simulated fraction ^b	45%	

Notes: ^a The 1-10 keV flux is relative to the power-law without considering the absorption. ^b this is the fraction of spectra simulated starting from a model derived from the MCMC with fit statistic larger than the best fit of the data. ^c The energy of the putative harmonic is fixed to be $2 \times E_{\text{Cyc1}}$.

for the description of the source continuum emission that are commonly exploited in case of strongly magnetized accreting NSs, as the Fermi-Dirac cutoff or the NPEX. None of these provide significant improvements over the phenomenological model and thus are not further discussed.

The *Swift*/BAT Transient Monitor⁵ ([Krimm et al. 2013](#)) shows that 4U 1700+24 was very active during 2014 and early 2015. Indeed, it triggered the BAT three times within four months. In this paper, we exploit the quasi-simultaneous BAT and XRT data collected during these triggers (see the complete log in Table 2) in order to perform an additional broad-band spectral analysis of the source beside that made possible by the previously reported *NuSTAR* data. The *Swift* data of 4U 1700+24 were uniformly processed and analysed using the standard software (FTOOLS⁶ v6.29b), calibra-

⁵ <https://swift.gsfc.nasa.gov/results/transients/weak/4U1700p24/>

⁶ https://heasarc.gsfc.nasa.gov/ftools/ftools_menu.html.

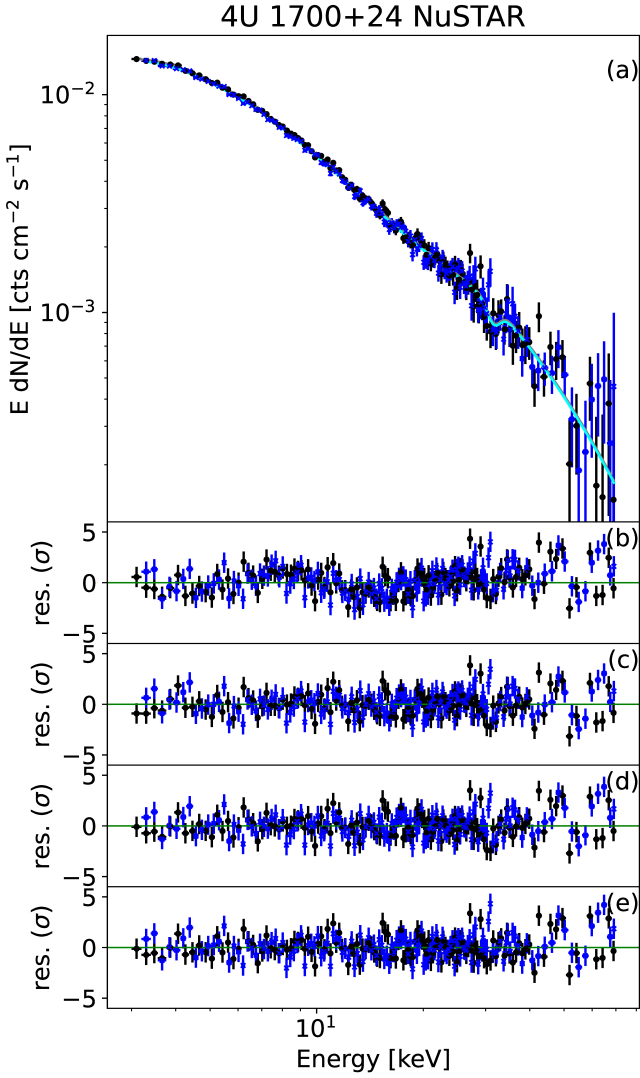


Figure 3. Panel (a): unfolded FPMA (black) and FPMB (blue) spectra of 4U 1700+24. The gray and cyan lines are the best-fit model for FPMA and FPMB, respectively, obtained by adopting the model $\text{TBabs}^*\text{gabs}^*\text{gabs}^*\text{highcut}^*\text{pegpwlw}$. Panel (b): residuals from the fit with the model $\text{TBabs}^*\text{highcut}^*\text{pegpwlw}$. Panel (c): residuals from the fit with the model $\text{TBabs}^*\text{highcut}^*(\text{bbodyrad}+\text{pegpwlw})$. Panel (d): residuals from the fit with the model $\text{TBabs}^*\text{gabs}^*\text{highcut}^*\text{pegpwlw}$. Panel (e): residuals from the fit with the model $\text{TBabs}^*\text{gabs}^*\text{gabs}^*\text{highcut}^*\text{pegpwlw}$. FPMA and FPMB data were rebinned here only for plotting purposes.

tion (CALDB⁷ 20210915), and methods. We analysed the BAT event data with the standard BAT software and created mask-tagged light curves for each trigger in the standard energy bands (15–25, 25–50, 50–100, 100–350 keV) rebinned so as to fulfill at least one of the following conditions: reaching a signal-to-noise ratio (S/N) of 5 or bin length of 10 s. Mask-weighted spectra were also extracted from the events collected during the first orbit of each observation (‘first orbit’ spectrum) and during the brightest part of the outburst⁸ (‘bright’ spectrum). An energy-dependent systematic error vector was applied

⁷ https://heasarc.gsfc.nasa.gov/docs/heasarc/caldb/caldb_intro.html.

⁸ We adopt the T_{total} baseline, that is the time over which all fluence is emitted, as calculated by `BATBLOCKS`.

to the data and response matrices were created with `BATDRMGEN` using the latest spectral redistribution matrices. The *Swift*/XRT data were filtered with the task `XRTPIPELINE` (v0.13.6). Data below 1 keV were discarded in order to avoid known instrumental residuals affecting the WT mode⁹. In the following, we analyse the observations corresponding to the different BAT triggers (ObsID 00612974000, 00621278000, and 00623434000), each consisting of three orbits of data. For each trigger, we selected a quasi-simultaneous pair of XRT and BAT spectra. Fits to each pair of spectra were performed using the same models discussed before for the *NuSTAR* data and including a constant to take into account both the difference of exposure and the non strict simultaneity of the XRT and BAT data.

4U 1700+24 triggered the BAT for the first time on 2014 September 17 at 13:30:35.5 UT (image trigger 612974, $T_0 = \text{MJD } 56917.56291043$; Burrows et al. 2014); *Swift* immediately slewed to the target so that the narrow field instruments (NFI) started observing the source at $T_0 + 1183$ s (see Table 2). During the observation ObsID 00612974000, the source was significantly detected in the BAT up to ~ 70 keV and the BAT lightcurve shows only a moderate variability. We checked that, when fit with a simple power-law, the first orbit spectrum and the bright spectrum ($T_0 + 524$ – 733 s) feature consistent parameters despite a difference by factor of two in flux. In the XRT, the source showed significant flux variability not corresponding to comparable variability in its spectral properties (as also noted by Burrows et al. 2014). The pile-up corrected count rate is seen to vary from a maximum of $\sim 70 \text{ c s}^{-1}$ to a minimum of $\sim 2 \text{ c s}^{-1}$ but the hardness ratio calculated in the 0.3–4 keV and 4–10 keV energy bands does not show significant variations. XRT data collected in the first and third orbit comprised only a few seconds of exposure, with the bulk of the photons collected during the second orbit. To maximize the signal-to-noise ratio, we thus considered for our broad-band spectral analysis only the quasi-simultaneous BAT bright spectrum ($T_0 + 524$ – 733 s) and the XRT/WT spectrum from the second orbit ($T_0 + 5634$ – 6188 s). A fit to these data using an absorbed power-law with an exponential cutoff ($\text{TBabs}^*\text{highcut}^*\text{pegpwlw}$) provided satisfactory results. We report in Table 2 the best-fit spectral parameters and the total χ^2 test statistics. By inspecting the residuals from the fit (see Fig. 4), we found no evidence for the presence of a black-body component. Due to the lack of energy coverage in the range 10–15 keV and the limited statistics of the BAT data around 30 keV, we could not evaluate the presence of the possible absorption features revealed by the fit to the *NuSTAR* data (see earlier in this section). We note, however, that the addition of two Gaussian absorption components with parameters fixed to those determined by *NuSTAR* did not cause a worsening of the fit and could thus be compatible with the XRT+BAT data.

The second outburst of the source occurred on 2014 December 13 at 01:56:11.09 UT (image trigger 621278, $T_0 = \text{MJD } 57004.08068392$; Kennea et al. 2014) and caused an immediate slew, so that the NFIs were on target at $T_0 + 120$ s. The properties of the *Swift* data of the first observation (ObsID 00621278000) are strikingly similar to those observed in the first trigger, with a remarkable X-ray variability and dynamic range (minimum to maximum ~ 5 – 10 c s^{-1}) associated with a substantially constant hardness ratio. Similarly to what was done for the first trigger, we only consider for our analysis the quasi-simultaneous BAT first orbit spectrum ($T_0 - 239$ s to $T_0 + 693$ s) and the XRT/WT first orbit spectrum ($T_0 + 120$ – 1561 s). The spectra were fit as was done above for the first trigger and we found compatible results (see Table 2). The same

⁹ https://www.swift.ac.uk/analysis/xrt/digest_cal.php.

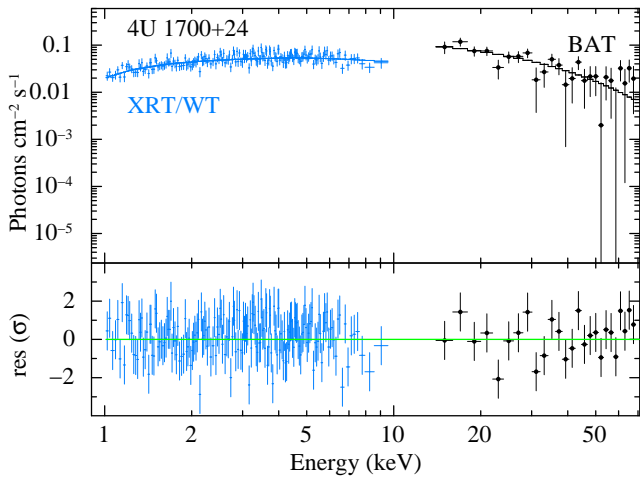


Figure 4. Spectroscopy of the 2014 September 17 outburst of 4U 1700+24 as recorded by *Swift*. Top panel: unfolded spectra of the nearly-simultaneous XRT/WT data (blue crosses) and BAT data (black circles) fit with the TBabs*highcut*pegpwlw model. Bottom panel: residuals from the fit.

conclusion concerning the presence of the black-body and the Gabs absorption components applies.

The third outburst of the source occurred a few days later on 2015 January 4 at 15:39:06.99 UT (image trigger 623434, T_0 =MJD 57026.65216427; Burrows et al. 2015) and caused an immediate slew, so that the NFIs were on target at T_0+406 s. The *Swift* data of the first observation (ObsID 00623434000) also show the X-ray variability and dynamic range (minimum to maximum ~ 5 –130 c s^{-1}) associated by a substantially constant hardness ratio. We only consider for our analysis the quasi-simultaneous BAT bright spectrum ($T_0 + 0$ –320 s) and the XRT/WT first orbit spectrum ($T_0 + 406$ –1818 s). The spectra were fit as was done above for the previous triggers, obtaining similar results and the same conclusions concerning additional spectral components beside the absorbed cut-off power-law (see Table 2). As both the combined XRT+BAT spectra of the second and third trigger were relatively similar to those of the first trigger, we did not show for brevity the corresponding images of the best fit models and residuals from the fits.

4 IGR J17329–2731

IGR J17329–2731 was discovered by *INTEGRAL* in 2017 (Postel et al. 2017) and rapidly pointed at with a number of different facilities giving rise to a prompt multi-wavelength campaign. Observations carried out with *XMM-Newton* and *NuSTAR* revealed the presence of prominent pulsations at a period of 6680 s and of a CRSF with a centroid energy of ~ 20 keV. These findings confirmed the presence of a NS accretor in this system endowed with a magnetic field of $2.4 \times 10^{12}(1+z)$ G, with z gravitation redshift at the NS surface. The positional accuracy provided by *Swift*/XRT allowed also for the identification of the optical counterpart through SOAR observations as a late M giant at a distance of $2.7^{+3.4}_{-1.2}$ kpc. IGR J17329–2731 was thus classified as a new member of the SyXBs (Bozzo et al. 2018; Bahramian et al. 2017). Although no pointed observation with sensitive X-ray telescopes was available before the discovery in 2017, Bozzo et al. (2018) used the entire available *INTEGRAL* archive to show that the source was likely never detectable before in the high energy domain and thus the ob-

servations carried out in 2017 might have as well discovered the very first moment when the source shone as a SyXB.

Following the discovery of the source, a long-term monitoring campaign was initiated with *Swift*/XRT in order to investigate the evolution of this object in the X-ray domain. In this paper, we report on the results of this concluded campaign. The *Swift* data of IGR J17329–2731 were uniformly processed and analysed using the standard software (FTOOLS¹⁰ v6.29b), calibration (CALDB¹¹ 20210915), and methods. The *Swift*/XRT data were filtered with the task XRTPIPELINE (v0.13.6). A log of all available XRT observations of IGR J17329–2731 is reported in Table 1.

We first extracted the source average count-rate for each observation in two energy bands, 0.5–4 keV and 4–10 keV, to compute the hardness-ratio (HR) reported also in Table 1. We then extracted for each observation the average spectrum of the source and fit it with a simple absorbed power-law model (the same as used in Sect. 2). We note that the XRT observations of IGR J17329–2731 are generally composed by 1 up to 3 snapshots with typical exposures of 300–1000 s. Therefore, none of the XRT observations is suitable to look for pulsations; furthermore the energy dependence of the pulse profile is unlikely to bias the HR value computed for each observation. The results of these analysis are summarized in Fig. 5.

The energy spectral distribution of the source in the XRT energy band is generally well described by simple absorbed power-law model, but there are intervals of time where the fits to the spectra with such simple model leave evident residuals around the typical energy of the neutral iron line at ~ 6.4 keV. During these intervals, the source is relatively faint and achieves a flux that is a factor of 5–10 lower than the surrounding time intervals. We also observe simultaneously during these intervals a flattening of the spectrum and a drop by a factor of few in the absorption column density, thus resembling what we usually observe in wind-fed systems during X-ray eclipses or obscuration events (see, e.g., Bozzo et al. 2009, and references therein). Although all spectral results are reported in Table 1, we also show a plot of the parameters as a function of time in Fig. 5 to ease the visual inspection. As it can be appreciated for this figure, the intervals corresponding to the obscuration events are concentrated during the second observational period (58150–58396 MJD) and occur in the time intervals separating the different source flares observed (4 flares are apparent in total during this period). The time interval characterized by the iron line with the largest equivalent width (≥ 2 keV) is centered around ~ 58240 MJD and it is also featuring the lowest recorded flux as well as one of the softest measured X-ray spectra. To illustrate the dramatic change in the source spectral properties between the emission during and outside the obscuration events, we show a comparison of typical spectra for the two cases in Fig. 6.

Although the uncertainties associated with the measurements of the iron line centroid energies in the different obscuration intervals in Table 1 is relatively large, we see also from Fig. 6 a marginal evidence for a change of the centroid between 6.4 keV up to 6.7 keV. In order to improve the measurements of the iron line, we thus stacked together all data collected during the obscuration intervals and obtained the spectrum that we show in Fig. 7. As expected based on the findings above, the spectrum appears relatively flat, and there is a prominent feature around 6.4 keV emerging from the residuals if the spectrum is fit with a simple absorbed powerlaw (in this case the result would be largely unacceptable with $\chi^2/d.o.f. = 147.5/45$).

¹⁰ https://heasarc.gsfc.nasa.gov/ftools/ftools_menu.html.

¹¹ https://heasarc.gsfc.nasa.gov/docs/heasarc/caldb/caldb_intro.html.

Table 2. *Swift*/XRT observation log of 4U 1700+24: observing sequence, date (MJD of the start of the observation), start and end times (UTC), XRT exposure time, and time since each BAT trigger for the start of the observation. We also indicated for each BAT+XRT spectral pair the value of the intercalibration constant, the absorption column density N_{H} , the powerlaw photon index Γ , and the flux in the 1–10 keV energy band (not corrected for absorption) determined from the spectral fit, as well as the values of the cutoff energy (E_{C}) and e-folding energy (E_{F}) of the (highecut) model.

Sequence	MJD	Start time (UT) (yyyy-mm-dd hh:mm:ss)	End time (UT) (yyyy-mm-dd hh:mm:ss)	Exposure (s)	Time since trigger (s)	C_2	N_{H} 10^{22} cm^{-2}	Γ	$F_{1-10 \text{ keV}}$ 10^{-11}	E_{C} keV	E_{F} keV	$\chi^2/\text{d.o.f.}$
00612974000 BAT	56917.56128	2014-09-17 13:28:15	2014-09-17 13:46:48	1113	-150	$2.64^{+0.84}_{-0.76}$	$0.37^{+0.12}_{-0.14}$	$0.93^{+0.12}_{-0.19}$	$79.6^{+0.08}_{-0.08}$	$4.5^{+1.4}_{-2.1}$	$19.6^{+7.5}_{-4.94}$	208.72/203
00612974000 WT	56917.57672	2014-09-17 13:50:28	2014-09-17 16:38:20	629	1183							
00621278000 BAT	57004.07803	2014-12-13 01:52:22	2014-12-13 05:37:37	13516	-239	$1.40^{+0.81}_{-0.52}$	$0.30^{+0.07}_{-0.07}$	$0.79^{+0.08}_{-0.09}$	$108.8^{+4.5}_{-3.7}$	$5.0^{+0.6}_{-0.5}$	$7.0^{+1.3}_{-1.0}$	501.32/471
00621278000 WT	57004.08219	2014-12-13 01:58:20	2014-12-13 06:38:33	2002	120							
00623434000 BAT	57026.64951	2015-01-04 15:35:18	2015-01-04 19:12:02	13195	-239	$1.27^{+0.43}_{-0.33}$	$0.23^{+0.06}_{-0.06}$	$0.71^{+0.05}_{-0.05}$	$210.6^{+11.2}_{-9.2}$	$3.87^{+0.57}_{-0.52}$	$11.3^{+2.8}_{-2.0}$	574.87/586
00623434000 WT	57026.65698	2015-01-04 15:46:02	2015-01-04 19:01:06	4656	406							

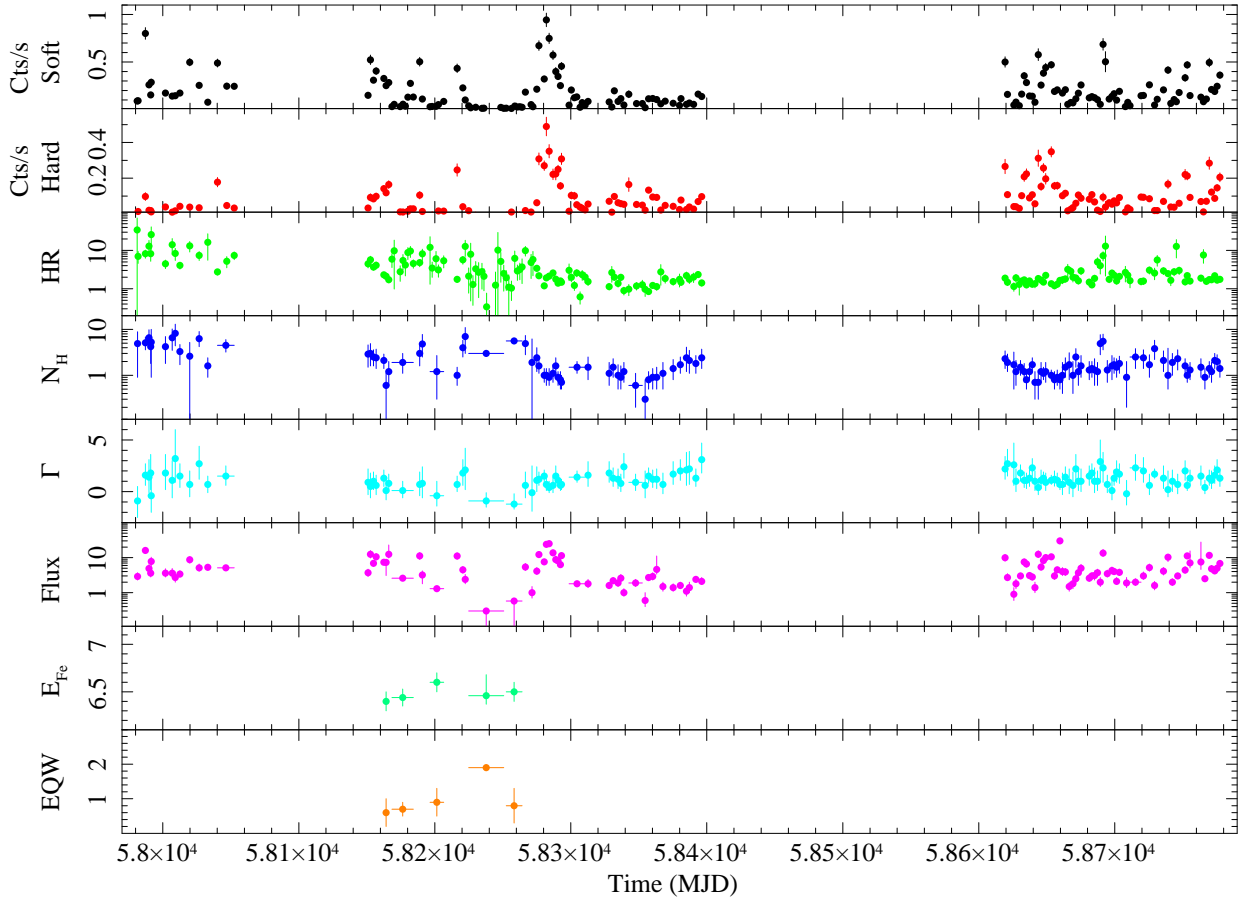


Figure 5. Plot of the energy resolved count-rate (soft is in 0.5–4 keV, while hard is 4–10 keV), HR, absorption column density, power-law photon index, flux, iron line centroid energy and equivalent width as a function of time obtained from the fit to the XRT data of IGR J17329–2731. Each point in the plot corresponds to one observation in the Table 1, unless observations have been stacked together as in the table to obtain a sufficient signal-to-noise ratio.

Adding a single thin Gaussian component (width fixed to zero) improves the fit ($\chi^2/\text{d.o.f.}=73.9/43$) but leaves significant residuals in the energy range 6.7–7.0 keV. Adding a second Gaussian component centered at 6.7 keV further improves the fit down to $\chi^2/\text{d.o.f.}=49.2/41$. From this fit, we measured an absorption column density of $N_{\text{H}}=(2.8^{+2.0}_{-1.4}) \times 10^{22} \text{ cm}^{-2}$, a powerlaw photon index of $\Gamma=-0.8 \pm 0.2$, and a 0.5–10 keV flux of $1.2 \times 10^{-11} \text{ erg cm}^{-2} \text{ s}^{-1}$ (not corrected for absorption). The measured centroid energies of the two iron lines in this case are $6.41 \pm 0.06 \text{ keV}$ and $6.8 \pm 0.1 \text{ keV}$.

The corresponding equivalent widths (EQWs) were $0.83^{+0.17}_{-0.40} \text{ keV}$ and $0.48^{+0.12}_{-0.40} \text{ keV}$, respectively. Although the fit is formally acceptable, we still noticed residuals around 7 keV. We thus attempted to add a third Gaussian line and obtained a centroid energy for this line of $6.9 \pm 0.1 \text{ keV}$ while all other parameters remained unchanged to within the uncertainties. The improvement of the fit with the third line is not statistically significant ($\chi^2/\text{d.o.f.}=39.6/39$), but it is interesting to note that the three lines correspond to the known predominant states of iron typically observed in wind-fed HMXBs (neutron

Table 1. *Swift*/XRT observation log for IGR J17329–2731. The OBSIDs starting with 0001024 are those already reported by Bozzo et al. (2018). In the table we also indicated for each observation the value of the absorption column density N_{H} , the powerlaw photon index Γ , and the flux in the 0.5–10 keV energy band (not corrected for absorption) determined from the spectral fit. We also reported, where needed, the values of the centroid energy (E_{Fe}) and equivalent width (EQW) of the neutron iron line energy. When values of the fit cover more than one row, it means that the corresponding observations have been merged together due to the otherwise too low number of counts to perform the spectral extraction.

Sequence	MJD	Start time (UT) (yyyy-mm-dd hh:mm:ss)	End time (UT) (yyyy-mm-dd hh:mm:ss)	Exposure (s)	N_{H} 10^{23} cm^{-2}	Γ	$F_{0.5-10 \text{ keV}}$ $10^{-11} \text{ erg cm}^{-2} \text{ s}^{-1}$	E_{Fe} keV	EQW keV	Cstat/d.o.f. ($\chi^2/\text{d.o.f.}$)
00010244001	57981.10361	2017-08-16 02:29:12	2017-08-16 02:45:47	1973	4.9 ± 4.0	$-0.9^{+1.4}_{-1.6}$	$2.9^{+0.8}_{-0.6}$			39.6/23
00010244002	57981.71182	2017-08-16 17:05:01	2017-08-16 20:02:18							
00010244003	57987.15883	2017-08-22 03:48:43	2017-08-22 05:29:59	985	$5.1^{+1.7}_{-1.5}$	$1.6^{+1.1}_{-1.0}$	16.0 ± 3.0			55.8/49
00010244004	57989.69705	2017-08-24 16:43:44	2017-08-24 23:10:53	893	$6.6^{+3.2}_{-2.7}$	$1.4^{+1.7}_{-1.5}$	$4.9^{+1.4}_{-0.9}$			28.8/26
00010244005	57990.95983	2017-08-25 23:02:08	2017-08-26 06:38:53	602	$4.2^{+2.8}_{-2.4}$	$1.8^{+1.8}_{-1.6}$	$3.6^{+1.2}_{-0.8}$			25.9/18
00010244006	57991.33843	2017-08-26 08:07:20	2017-08-26 14:58:53	865	$5.3^{+4.7}_{-4.4}$	$-0.4^{+1.7}_{-1.6}$	$7.8^{+2.5}_{-2.0}$			13.7/15
00010244007	58001.89720	2017-09-05 21:31:57	2017-09-05 23:16:53	659	$4.2^{+2.8}_{-2.4}$	$1.8^{+1.8}_{-1.6}$	$3.6^{+1.2}_{-0.8}$			25.9/18
00010244008	58006.94238	2017-09-10 22:37:01	2017-09-10 22:52:54	953	$6.6^{+3.6}_{-3.1}$	$1.1^{+1.9}_{-1.7}$	$3.6^{+1.3}_{-0.9}$			18.0/19
00010244009	58009.06811	2017-09-13 01:38:04	2017-09-13 06:27:52	717	$8.2^{+4.8}_{-3.8}$	$3.2^{+2.8}_{-2.3}$	$2.7^{+1.2}_{-0.7}$			19.7/14
00010244010	58012.53078	2017-09-16 12:44:19	2017-09-16 13:01:52	1053	$3.3^{+1.4}_{-1.6}$	$1.5^{+1.2}_{-1.1}$	$3.4^{+0.8}_{-0.6}$			51.8/29
00010244011	58019.63368	2017-09-23 15:12:29	2017-09-23 21:47:54	898	$2.6^{+2.6}_{-2.7}$	$0.7^{+1.3}_{-1.2}$	$8.7^{+1.9}_{-1.7}$			23.3/26
00010244012	58026.68470	2017-09-30 16:25:57	2017-09-30 16:41:53	955	$6.3^{+2.7}_{-2.1}$	$2.7^{+1.7}_{-1.5}$	$5.1^{+1.5}_{-1.0}$			32.2/36
00010244013	58033.05169	2017-10-07 01:14:26	2017-10-07 02:56:53	1508	$1.6^{+0.8}_{-0.7}$	0.7 ± 0.8	$5.3^{+1.1}_{-0.9}$			72.8/44
00010244014	58040.16153	2017-10-14 03:52:36	2017-10-14 04:02:53							
00010244015	58047.01855	2017-10-21 00:26:42	2017-10-21 01:55:44							
00010244016	58052.52036	2017-10-26 12:29:18	2017-10-26 12:44:54	1381	$4.5^{+1.5}_{-1.3}$	$1.5^{+1.0}_{-0.9}$	5.1 ± 0.8			53.7/57
00010381001	58150.88910	2018-02-01 21:20:17	2018-02-01 21:36:53	995	$2.9^{+1.7}_{-1.4}$	$0.9^{+1.3}_{-1.2}$	$3.7^{+1.0}_{-0.8}$			104.7/131
00010381002	58152.68608	2018-02-03 16:27:56	2018-02-03 16:43:52	955	$3.0^{+1.9}_{-1.4}$	$0.5^{+1.3}_{-1.1}$	$12.5^{+3.4}_{-2.7}$			95.0/115
00010381003	58154.94023	2018-02-05 22:33:55	2018-02-05 22:51:53	1078	$2.5^{+1.1}_{-0.9}$	$1.0^{+0.9}_{-0.8}$	$6.9^{+1.4}_{-1.2}$			107.2/183
00010381004	58156.87057	2018-02-07 20:53:36	2018-02-07 21:08:52	915	$2.4^{+1.3}_{-1.0}$	$0.6^{+1.0}_{-0.9}$	$10.6^{+2.4}_{-2.0}$			124.5/158
00010381005	58162.51007	2018-02-13 12:14:30	2018-02-13 12:30:53	983	$2.1^{+0.8}_{-0.7}$	$1.3^{+0.8}_{-0.8}$	$7.4^{+1.4}_{-1.1}$			180.2/209
00010381006	58164.16929	2018-02-15 04:03:46	2018-02-15 04:19:51	965	$0.6^{+0.5}_{-0.6}$	$0.1^{+1.1}_{-0.9}$	$7.3^{+0.3}_{-0.2}$	$6.4^{+0.1}_{-0.1}$	$0.6^{+0.4}_{-0.4}$	(6.9/11)
00010381007	58166.16069	2018-02-17 03:51:23	2018-02-17 04:07:53	990	$1.2^{+0.8}_{-0.6}$	$0.8^{+0.9}_{-0.8}$	$12.5^{+10.5}_{-2.7}$			123.0/148
00010381008	58168.48439	2018-02-19 11:37:31	2018-02-19 12:13:39							
00010381009	58170.14349	2018-02-21 03:26:37	2018-02-21 03:42:52							
00010381011	58174.52953	2018-02-25 12:42:31	2018-02-25 12:58:54							
00010381012	58176.58920	2018-02-27 14:08:26	2018-02-27 14:23:54							
00010381013	58178.31495	2018-03-01 07:33:31	2018-03-01 07:48:54	8834	$1.9^{+1.1}_{-0.8}$	$0.1^{+0.9}_{-0.7}$	2.6 ± 0.2	$6.44^{+0.09}_{-0.09}$	$0.7^{+0.2}_{-0.2}$	(20.7/19)
00010381014	58180.24239	2018-03-03 05:49:02	2018-03-03 06:03:52							
00010381015	58182.03505	2018-03-05 00:50:27	2018-03-05 01:07:53							
00010381016	58184.22645	2018-03-07 05:26:05	2018-03-07 05:41:52							
00010381017	58188.87579	2018-03-11 21:01:08	2018-03-11 21:17:53	1005	$3.0^{+1.8}_{-1.4}$	$0.7^{+1.2}_{-1.1}$	$11.2^{+2.8}_{-2.3}$			134.3/132
00010381018	58190.80228	2018-03-13 19:15:16	2018-03-13 19:33:52	1116	$4.8^{+3.0}_{-2.3}$	$0.8^{+1.6}_{-1.4}$	$3.2^{+1.0}_{-1.4}$			72.42/95
00010381020	58196.51638	2018-03-19 12:23:35	2018-03-19 12:38:52							
00010381021	58198.03978	2018-03-21 00:57:17	2018-03-21 01:14:52							
00010381022	58200.90118	2018-03-23 21:37:42	2018-03-23 21:54:52	4705	$1.2^{+1.5}_{-0.9}$	$-0.4^{+1.4}_{-1.0}$	1.3 ± 0.1	$6.6^{+0.1}_{-0.1}$	$0.9^{+0.4}_{-0.4}$	(4.8/7)
00010381023	58202.63502	2018-03-25 15:14:25	2018-03-25 15:28:53							
00010381025	58206.54025	2018-03-29 12:57:57	2018-03-29 13:11:52							
00010381029	58216.36885	2018-04-08 08:51:08	2018-04-08 09:09:53	1126	$1.0^{+0.5}_{-0.4}$	$0.7^{+0.8}_{-0.7}$	$11.1^{+2.6}_{-2.1}$			114.1/141
00010381031	58220.62044	2018-04-12 14:53:25	2018-04-12 15:11:54	1108	$4.0^{+1.8}_{-1.5}$	$1.8^{+1.3}_{-1.2}$	$4.5^{+1.1}_{-0.9}$			99.4/143
00010381032	58222.34786	2018-04-14 08:20:54	2018-04-14 08:36:52	958	$7.0^{+4.0}_{-4.0}$	$2.1^{+2.1}_{-1.9}$	$2.4^{+0.9}_{-0.6}$			57.7/80
00010381033	58224.87328	2018-04-16 20:57:31	2018-04-16 21:01:52							
00010381034	58226.40209	2018-04-18 09:39:00	2018-04-18 09:54:53							
00010381035	58228.00227	2018-04-20 00:03:15	2018-04-20 00:17:52							
00010381036	58230.12174	2018-04-22 02:55:17	2018-04-22 03:10:53							
00010381037	58232.24687	2018-04-24 05:55:29	2018-04-24 06:10:52							
00010381038	58234.63747	2018-04-26 15:17:57	2018-04-26 15:34:52							
00010381039	58236.10438	2018-04-28 02:30:18	2018-04-28 02:45:53	10659	< 3.0	$-0.9^{+0.8}_{-0.6}$	$0.30^{+0.05}_{-0.25}$	$6.46^{+0.22}_{-0.09}$	$1.9^{+0.07}_{-0.08}$	19.8/26
00010381040	58238.10514	2018-04-30 02:31:24	2018-04-30 02:46:52							
00010381041	58244.66515	2018-05-06 15:57:49	2018-05-06 16:13:51							
00010381042	58246.39222	2018-05-08 09:24:47	2018-05-08 11:08:53							
00010381043	58248.51643	2018-05-10 12:23:39	2018-05-10 12:39:52							
00010381044	58250.64859	2018-05-12 15:33:57	2018-05-12 15:49:53							

iron line at 6.4 keV, He-like iron line at 6.7 keV, and H-like iron line at 6.9 keV; see, e.g., Fürst et al. 2011; Liu et al. 2018, and references therein). For completeness, we mention that the residuals around the iron line complex could also be alternatively fit ($\chi^2/\text{d.o.f.}=40.1/42$) with a single large Gaussian component (leaving the continuum parameters virtually unchanged). In this case, the centroid energy

would be 6.52 ± 0.06 keV and the line width 0.27 ± 0.07 keV. We consider this fit unphysical as the centroid energy of the line would only be marginally compatible with the neutral iron value and a broadening of the line would only be expected in case of a fast rotating accretion disk around a weakly magnetized NS (see, e.g., Di Salvo & Sanna 2020, for a recent review) but not in a wind-fed

Table 1. Continued.

Sequence	MJD	Start time (UT) (yyyy-mm-dd hh:mm:ss)	End time (UT) (yyyy-mm-dd hh:mm:ss)	Exposure (s)	N_{H} 10^{23} cm^{-2}	Γ	$F_{0.5-10 \text{ keV}}$ $10^{-11} \text{ erg cm}^{-2} \text{ s}^{-1}$	E_{Fe} keV	EQW keV	Cstat/d.o.f.
00010381045	58252.50513	2018-05-14 12:07:23	2018-05-14 12:24:53							
00010381046	58254.43585	2018-05-16 10:27:37	2018-05-16 10:43:52							
00010381047	58256.36750	2018-05-18 08:49:12	2018-05-18 09:05:52							
00010381048	58258.82480	2018-05-20 19:47:42	2018-05-20 20:03:52	6907	< 5.6	$-1.2^{+1.0}_{-0.5}$	$0.58^{+0.05}_{-0.54}$	$6.5^{+0.1}_{-0.1}$	$0.8^{+0.5}_{-0.5}$	18.6/27
00010381049	58260.74879	2018-05-22 17:58:15	2018-05-22 18:15:53							
00010381050	58262.46195	2018-05-24 11:05:12	2018-05-24 11:20:52							
00010381051	58264.18867	2018-05-26 04:31:41	2018-05-26 04:46:54							
00010381052	58266.58874	2018-05-28 14:07:46	2018-05-28 14:24:52	1025	$4.9^{+2.5}_{-2.1}$	$0.6^{+1.3}_{-1.2}$	$5.4^{+1.4}_{-1.1}$			106.5/131
00010381053	58270.84194	2018-06-01 20:12:23	2018-06-01 20:30:54	2061	$1.9^{+4.3}_{-1.8}$	$-0.1^{+2.6}_{-1.8}$	$1.0^{+0.5}_{-0.3}$			42.2/42
00010381054	58272.16777	2018-06-03 04:01:35	2018-06-03 04:17:53							
00010381055	58274.96290	2018-06-05 23:06:34	2018-06-05 23:22:52	978	$2.4^{+1.6}_{-1.2}$	$1.1^{+1.3}_{-1.1}$	$4.1^{+1.1}_{-0.8}$			110.4/146
00010381056	58276.54765	2018-06-07 13:08:36	2018-06-07 15:03:52	890	$1.6^{+0.6}_{-0.5}$	$1.2^{+0.7}_{-0.6}$	$12.2^{+2.1}_{-1.8}$			202.4/217
00010381057	58280.46373	2018-06-11 11:07:46	2018-06-11 11:25:54	1088	$1.0^{+0.4}_{-0.3}$	$1.5^{+0.6}_{-0.6}$	$7.6^{+1.4}_{-1.1}$			192.4/191
00010381058	58282.05881	2018-06-13 01:24:40	2018-06-13 01:40:53	973	$1.0^{+0.4}_{-0.3}$	$0.7^{+0.6}_{-0.5}$	$24.0^{+4.0}_{-4.0}$			176.0/225
00010381059	58284.05580	2018-06-15 01:20:20	2018-06-15 01:36:53	993	$0.9^{+0.5}_{-0.3}$	$0.4^{+0.6}_{-0.5}$	$25.0^{+5.0}_{-3.0}$			173.8/251
00010381060	58286.90682	2018-06-17 21:45:49	2018-06-17 22:00:52	903	$1.1^{+0.6}_{-0.4}$	$0.6^{+0.8}_{-0.7}$	$13.7^{+2.8}_{-2.3}$			148.5/176
00010381061	58288.97411	2018-06-19 23:22:43	2018-06-19 23:37:53	910	$1.6^{+0.8}_{-0.6}$	$1.5^{+1.0}_{-0.9}$	$8.8^{+2.3}_{-1.8}$			110.8/118
00010381062	58290.37278	2018-06-21 08:56:35	2018-06-21 18:43:52	1171	$0.9^{+0.3}_{-0.3}$	$1.1^{+0.6}_{-0.5}$	$8.1^{+1.4}_{-1.1}$			179.6/237
00010381063	58292.35199	2018-06-23 08:26:52	2018-06-23 08:42:52	960	$0.8^{+0.4}_{-0.3}$	$0.6^{+0.6}_{-0.5}$	$6.3^{+1.2}_{-1.0}$			147.1/197
00010381064	58293.14907	2018-06-24 03:34:39	2018-06-24 03:45:53	674	$0.7^{+0.3}_{-0.2}$	$0.7^{+0.5}_{-0.5}$	$11.4^{+2.0}_{-1.7}$			162.1/219
00010381065	58298.73917	2018-06-29 17:44:24	2018-06-29 17:53:53							
00010381066	58300.40880	2018-07-01 09:48:40	2018-07-01 11:14:53							
00010381067	58302.58538	2018-07-03 14:02:56	2018-07-03 15:38:52							
00010381068	58304.32606	2018-07-05 07:49:31	2018-07-05 09:25:54	4679	$1.5^{+0.5}_{-0.4}$	$1.4^{+0.6}_{-0.5}$	$1.8^{+0.3}_{-0.2}$			239.5/285
00010381069	58306.78253	2018-07-07 18:46:50	2018-07-07 20:13:54							
00010381070	58308.36775	2018-07-09 08:49:33	2018-07-09 09:01:52							
00010381071	58310.49337	2018-07-11 11:50:26	2018-07-11 12:06:52							
00010381072	58312.68326	2018-07-13 16:23:53	2018-07-13 16:41:54	1081	$1.5^{+1.0}_{-0.7}$	$1.6^{+1.3}_{-1.1}$	$1.8^{+0.6}_{-0.4}$			80.9/94
00010381074	58328.21535	2018-07-29 05:10:06	2018-07-29 05:28:52	1126	$1.1^{+0.8}_{-0.5}$	$1.8^{+1.1}_{-0.9}$	$1.6^{+0.4}_{-0.3}$			73.8/110
00010381075	58330.14540	2018-07-31 03:29:22	2018-07-31 05:12:53							
00010381076	58332.01371	2018-08-02 00:19:44	2018-08-02 00:35:52	1983	$1.5^{+0.8}_{-0.6}$	$1.3^{+1.0}_{-0.8}$	$2.2^{+0.5}_{-0.4}$			130.5/148
00010381077	58334.73540	2018-08-04 17:38:58	2018-08-04 17:56:54	1076	$1.0^{+0.7}_{-0.5}$	$1.2^{+1.0}_{-0.9}$	$1.9^{+0.6}_{-0.4}$			87.5/101
00010381078	58336.79321	2018-08-06 19:02:13	2018-08-06 19:19:54	1061	$0.9^{+0.7}_{-0.4}$	$0.8^{+0.9}_{-0.8}$	$2.6^{+0.7}_{-0.5}$			98.1/124
00010381079	58339.04198	2018-08-09 01:00:27	2018-08-09 01:16:52	985	$1.2^{+0.7}_{-0.5}$	$2.4^{+1.3}_{-1.1}$	$1.0^{+0.3}_{-0.2}$			73.7/72
00010381080	58342.69665	2018-08-12 16:43:10	2018-08-12 16:46:53							
00010381081	58348.28656	2018-08-18 06:52:39	2018-08-18 07:07:54	1682	$0.6^{+0.5}_{-0.4}$	$0.9^{+0.8}_{-0.8}$	$1.9^{+0.5}_{-0.4}$			126.2/139
00010381082	58352.59571	2018-08-22 14:17:49	2018-08-22 14:26:53							
00010381083	58354.39100	2018-08-24 09:23:02	2018-08-24 22:29:52	1066	$0.3^{+0.5}_{-0.2}$	$0.6^{+1.4}_{-1.2}$	$0.6^{+0.4}_{-0.2}$			49.9/33
00010381084	58357.17574	2018-08-27 04:13:03	2018-08-27 05:56:53	1038	$0.8^{+0.4}_{-0.3}$	$1.5^{+0.8}_{-0.7}$	$2.7^{+0.6}_{-0.5}$			125.9/151
00010381085	58360.23100	2018-08-30 05:32:38	2018-08-30 05:49:53	1036	$0.9^{+0.5}_{-0.4}$	$1.2^{+0.9}_{-0.8}$	$2.9^{+0.8}_{-0.6}$			120.3/146
00010381086	58363.14928	2018-09-02 03:34:57	2018-09-02 03:48:52	832	$0.9^{+0.6}_{-0.4}$	$1.2^{+1.0}_{-0.9}$	$4.6^{+6.5}_{-1.2}$			118.0/98
00010381087	58366.13522	2018-09-05 03:14:43	2018-09-05 03:19:16							
00010381088	58369.39329	2018-09-08 09:26:20	2018-09-08 09:44:53	1385	$1.1^{+0.8}_{-0.6}$	$0.7^{+1.1}_{-0.9}$	$1.5^{+0.5}_{-0.4}$			76.7/83
00010381089	58375.16760	2018-09-14 04:01:20	2018-09-14 08:55:53	1271	$1.4^{+0.8}_{-0.6}$	$1.7^{+1.2}_{-1.0}$	$1.4^{+0.4}_{-0.3}$			90.3/98
00010381090	58379.95453	2018-09-18 22:54:30	2018-09-18 23:09:53							
00010381091	58381.01428	2018-09-20 00:20:33	2018-09-20 02:14:52	1938	$1.7^{+0.8}_{-0.6}$	$2.0^{+1.1}_{-0.9}$	$1.6^{+0.4}_{-0.3}$			136.3/147
00010381092	58384.07019	2018-09-23 01:41:04	2018-09-24 21:08:52	1447	$2.4^{+1.7}_{-1.2}$	$2.1^{+1.7}_{-1.2}$	$1.1^{+0.4}_{-0.3}$			81.6/81
00010381093	58387.19114	2018-09-26 04:35:14	2018-09-26 04:52:52	1058	$2.1^{+1.4}_{-1.0}$	$2.2^{+1.7}_{-1.5}$	$1.4^{+0.6}_{-0.4}$			60.2/79
00010381094	58390.25699	2018-09-29 06:10:04	2018-09-29 06:25:54							
00010381095	58393.43297	2018-10-02 10:23:28	2018-10-02 18:29:53	2166	$1.8^{+0.9}_{-0.7}$	$1.3^{+0.9}_{-0.8}$	$2.4^{+0.5}_{-0.4}$			165.7/178
00010381096	58396.22600	2018-10-05 05:25:26	2018-10-05 05:41:52	985	$2.4^{+1.3}_{-1.0}$	$3.1^{+1.6}_{-1.3}$	$2.1^{+0.6}_{-0.4}$			98.3/118
00010381097	58619.35967	2019-05-16 08:37:55	2019-05-16 08:51:52	837	$2.3^{+1.1}_{-0.9}$	$2.2^{+1.2}_{-1.0}$	$9.9^{+2.5}_{-1.9}$			124.1/116
00010381098	58621.08933	2019-05-18 02:08:38	2019-05-18 02:23:53	915	$1.9^{+1.0}_{-0.7}$	$2.7^{+1.4}_{-1.2}$	$2.7^{+0.8}_{-0.5}$			116.3/113
00010381099	58625.72455	2019-05-22 17:23:21	2019-05-22 17:39:54	993	$1.7^{+1.5}_{-1.2}$	$2.6^{+2.1}_{-2.0}$	$0.9^{+0.5}_{-0.3}$			38.5/58
00010381100	58627.31490	2019-05-24 07:33:27	2019-05-24 07:48:52	925	$1.2^{+0.9}_{-0.6}$	$1.0^{+1.2}_{-1.0}$	$1.8^{+0.6}_{-0.5}$			72.5/77
00010381101	58629.78721	2019-05-26 18:50:38	2019-05-26 19:06:54							
00010381102	58631.49904	2019-05-28 11:58:37	2019-05-28 12:16:53	1429	$1.5^{+0.6}_{-0.5}$	$1.8^{+0.8}_{-0.8}$	$3.0^{+0.6}_{-0.5}$			106.5/182
00010381103	58633.35948	2019-05-30 08:37:38	2019-05-30 08:54:51	1033	$1.2^{+0.6}_{-0.5}$	$1.1^{+0.8}_{-0.7}$	$7.5^{+1.7}_{-1.4}$			142.8/160
00010381104	58635.03407	2019-06-01 00:49:03	2019-06-01 01:04:54	950	$0.8^{+0.4}_{-0.3}$	$1.1^{+0.7}_{-0.8}$	$6.6^{+1.5}_{-1.2}$			123.3/153
00010381105	58637.27834	2019-06-03 06:40:48	2019-06-03 06:58:54	1086	$1.2^{+0.6}_{-0.4}$	$1.3^{+0.9}_{-0.8}$	$3.1^{+0.7}_{-0.6}$			123.3/145

young pulsar as that hosted in IGR J17329–2731 (see the discussion in Torrejón et al. 2010).

5 DISCUSSION

We reported in this paper about the broad-band X-ray spectroscopy of two of the few known SyXBs, Sct X–1, and 4U 1700+24. We have been looking specifically for the presence of CRSFs in their spectral energy distribution that could point toward the presence

Table 1. Continued.

Sequence	MJD	Start time (UT) (yyyy-mm-dd hh:mm:ss)	End time (UT) (yyyy-mm-dd hh:mm:ss)	Exposure (s)	N_{H} 10^{23} cm^{-2}	Γ	$F_{0.5-10 \text{ keV}}$ $10^{-11} \text{ erg cm}^{-2} \text{ s}^{-1}$	E_{Fe} keV	EQW keV	Cstat/d.o.f.
00010381106	58639.34760	2019-06-05 08:20:32	2019-06-05 08:38:53	1101	$1.7^{+0.7}_{-0.5}$	$2.3^{+0.9}_{-0.8}$	$2.8^{+0.6}_{-0.5}$			116.2/149
00010381107	58641.34120	2019-06-07 08:11:19	2019-06-07 08:24:52	812	$0.7^{+0.5}_{-0.4}$	$1.0^{+1.0}_{-0.9}$	$1.4^{+0.6}_{-0.4}$			74.2/77
00010381108	58643.72603	2019-06-09 17:25:29	2019-06-09 17:43:52	1103	$0.7^{+0.6}_{-0.4}$	$0.4^{+0.8}_{-0.7}$	$12.5^{+3.2}_{-2.5}$			136.0/119
00010381109	58645.78926	2019-06-11 18:56:32	2019-06-11 19:13:52	725	$1.2^{+0.7}_{-0.5}$	$1.1^{+1.0}_{-0.8}$	$5.4^{+1.3}_{-1.0}$			114.7/135
00010381110	58647.57200	2019-06-13 13:43:41	2019-06-13 14:01:54	1093	$1.1^{+0.4}_{-0.3}$	$1.3^{+0.6}_{-0.6}$	$8.3^{+1.4}_{-1.2}$			208.7/211
00010381111	58649.23274	2019-06-15 05:35:08	2019-06-15 05:51:54	1005	$1.2^{+0.7}_{-0.5}$	$0.9^{+0.9}_{-0.8}$	$10.0^{+2.4}_{-2.0}$			130.7/139
00010381112	58653.34838	2019-06-19 08:21:39	2019-06-19 08:37:52	973	$1.0^{+0.3}_{-0.2}$	$1.1^{+0.5}_{-0.4}$	$10.6^{+1.4}_{-1.2}$			251.5/319
00010381113	58655.67261	2019-06-21 16:08:33	2019-06-21 16:24:54	980	$0.8^{+0.4}_{-0.3}$	$1.2^{+0.8}_{-0.7}$	$3.0^{+0.8}_{-0.6}$			104.5/122
00010381114	58657.66776	2019-06-23 16:01:34	2019-06-23 16:18:52	1038	$0.9^{+0.4}_{-0.3}$	$1.1^{+0.7}_{-0.6}$	$4.5^{+0.9}_{-0.8}$			123.8/170
00010381115	58659.60588	2019-06-25 14:32:28	2019-06-25 14:47:53	925	$0.8^{+0.3}_{-0.3}$	$0.7^{+0.5}_{-0.5}$	$30.0^{+5.0}_{-5.0}$			198.0/217
00010381116	58661.46622	2019-06-27 11:11:21	2019-06-27 11:24:53	634	$1.0^{+0.9}_{-0.6}$	$0.7^{+1.1}_{-1.0}$	$4.0^{+1.2}_{-0.9}$			94.6/96
00010381117	58663.65581	2019-06-29 15:44:22	2019-06-29 15:59:52	930	$1.5^{+0.9}_{-0.6}$	$1.4^{+1.0}_{-0.9}$	$3.9^{+1.0}_{-0.8}$			91.9/123
00010381118	58665.37906	2019-07-01 09:05:50	2019-07-01 09:19:53	1775	$1.7^{+1.4}_{-0.9}$	$0.9^{+1.3}_{-1.1}$	$1.5^{+0.5}_{-0.4}$			75.3/109
00010381119	58667.63913	2019-07-03 15:20:20	2019-07-03 15:35:53	890	$1.0^{+1.0}_{-0.6}$	$0.6^{+1.3}_{-1.1}$	$1.8^{+0.7}_{-0.5}$			45.8/68
00010381120	58669.23266	2019-07-05 05:35:02	2019-07-05 05:49:52	865	$2.5^{+1.3}_{-1.0}$	$2.2^{+1.4}_{-1.0}$	$2.5^{+0.8}_{-0.6}$			90.3/99
00010381121	58671.35797	2019-07-07 08:35:29	2019-07-07 08:49:54	948	$1.2^{+0.7}_{-0.6}$	$1.0^{+1.0}_{-0.9}$	$3.7^{+1.0}_{-0.8}$			123.7/131
00010381122	58673.21462	2019-07-09 05:09:02	2019-07-09 05:24:53	975	$1.6^{+1.1}_{-0.7}$	$1.0^{+1.2}_{-1.1}$	$5.0^{+1.4}_{-1.1}$			83.1/116
00010381123	58675.20600	2019-07-11 04:56:38	2019-07-11 05:12:53	975	$1.3^{+0.7}_{-0.5}$	$1.5^{+1.0}_{-0.9}$	$2.6^{+0.7}_{-0.5}$			84.2/122
00010381124	58681.18158	2019-07-17 04:21:28	2019-07-17 04:37:53	985	$1.4^{+0.6}_{-0.5}$	$1.8^{+0.9}_{-0.8}$	$3.0^{+0.7}_{-0.6}$			125.8/142
00010381125	58683.17534	2019-07-19 04:12:29	2019-07-19 04:26:54	865	$1.3^{+1.0}_{-0.7}$	$1.0^{+1.3}_{-1.1}$	$3.1^{+1.1}_{-0.8}$			64.2/96
00010381126	58685.10042	2019-07-21 02:24:35	2019-07-21 02:35:57	682	$1.2^{+0.7}_{-0.6}$	$1.0^{+1.0}_{-0.9}$	$3.7^{+1.0}_{-0.8}$			123.7/131
00010381127	58687.29223	2019-07-23 07:00:48	2019-07-23 07:16:53	965	$1.2^{+0.7}_{-0.6}$	$1.0^{+1.0}_{-0.9}$	$3.7^{+1.0}_{-0.8}$			123.7/131
00010381128	58689.33925	2019-07-25 08:08:30	2019-07-25 09:54:53	820	$4.9^{+2.8}_{-2.1}$	$2.9^{+2.1}_{-1.7}$	$2.0^{+0.7}_{-0.5}$			57.8/90
00010381129	58691.41148	2019-07-27 09:52:31	2019-07-27 10:07:54	923	$5.5^{+2.4}_{-1.9}$	$2.3^{+1.7}_{-1.4}$	$13.5^{+3.6}_{-2.7}$			123.5/130
00010381130	58693.12654	2019-07-29 03:02:12	2019-07-29 03:04:53	1098	$1.3^{+0.8}_{-0.6}$	$0.7^{+0.9}_{-0.8}$	$3.5^{+0.9}_{-0.7}$			104.0/136
00010381131	58695.85434	2019-07-31 20:30:15	2019-07-31 20:45:52	953	$1.6^{+1.1}_{-0.8}$	$0.1^{+1.0}_{-0.9}$	$4.3^{+1.1}_{-0.9}$			120.8/125
00010381132	58697.91528	2019-08-02 21:57:59	2019-08-02 22:13:52	1091	$1.7^{+0.7}_{-0.6}$	$1.3^{+0.8}_{-0.7}$	$4.0^{+0.8}_{-0.7}$			171.0/175
00010381133	58699.44008	2019-08-04 10:33:43	2019-08-04 10:51:53	1091	$1.5^{+0.8}_{-0.6}$	$1.9^{+1.1}_{-1.0}$	$2.1^{+0.6}_{-0.4}$			99.7/119
00010381134	58701.36509	2019-08-06 08:45:43	2019-08-06 09:03:54	895	$1.8^{+0.8}_{-0.7}$	$1.7^{+1.0}_{-0.9}$	$3.8^{+0.9}_{-0.7}$			125.7/139
00010381135	58703.43123	2019-08-08 10:20:58	2019-08-08 10:35:53	1810	$0.9^{+1.1}_{-0.7}$	$-0.2^{+1.3}_{-1.1}$	$1.9^{+0.8}_{-0.5}$			97.8/100
00010381136	58707.74719	2019-08-12 17:55:57	2019-08-12 18:09:52	1427	$2.5^{+1.3}_{-1.1}$	$2.3^{+1.3}_{-1.2}$	$2.0^{+0.5}_{-0.4}$			113.0/138
00010381137	58709.53237	2019-08-14 12:46:36	2019-08-14 13:02:52	993	$2.4^{+1.2}_{-1.0}$	$2.0^{+1.3}_{-1.1}$	$3.0^{+0.9}_{-0.6}$			102.1/114
00010381138	58711.19394	2019-08-16 04:39:16	2019-08-16 04:50:28	915	$1.7^{+1.1}_{-0.8}$	$0.6^{+1.1}_{-0.9}$	$5.2^{+1.4}_{-1.1}$			86.6/119
00010381139	58719.28919	2019-08-24 06:56:26	2019-08-24 07:09:00	2008	$3.8^{+2.0}_{-1.6}$	$1.7^{+0.5}_{-0.4}$	$1.6^{+0.5}_{-0.4}$			87.5/122
00010381140	58721.08657	2019-08-26 02:04:39	2019-08-26 02:19:52	878	$2.1^{+1.3}_{-0.9}$	$1.3^{+1.2}_{-1.0}$	$4.1^{+1.1}_{-0.9}$			95.4/114
00010381141	58722.27516	2019-09-01 06:36:13	2019-09-01 06:39:51	970	$1.0^{+2.9}_{-0.5}$	$0.2^{+1.8}_{-0.7}$	$10.3^{+2.2}_{-2.6}$			155.9/165
00010381142	58725.40668	2019-08-30 09:45:36	2019-08-30 10:00:51	2016	$1.9^{+1.1}_{-0.9}$	$1.0^{+1.1}_{-1.0}$	$2.0^{+0.5}_{-0.4}$			132.1/148
00010381143	58727.27516	2019-09-01 06:36:13	2019-09-01 06:39:51	1848	$2.3^{+1.3}_{-1.0}$	$0.7^{+1.0}_{-0.9}$	$3.0^{+0.6}_{-0.5}$			152.3/163
00010381144	58731.24285	2019-09-05 05:49:42	2019-09-05 06:04:52	970	$1.6^{+0.7}_{-0.6}$	$2.0^{+1.0}_{-0.9}$	$4.4^{+1.1}_{-0.8}$			120.1/124
00010381145	58733.83353	2019-09-09 20:00:16	2019-09-09 20:14:54	857	$1.0^{+0.4}_{-0.3}$	$0.6^{+0.5}_{-0.5}$	$11.2^{+1.7}_{-1.4}$			213.4/280
00010381146	58739.15327	2019-09-13 03:40:42	2019-09-13 03:56:53	1116	$1.3^{+0.6}_{-0.5}$	$1.3^{+0.8}_{-0.7}$	$7.1^{+8.4}_{-2.0}$			149.3/163
00010381147	58741.14633	2019-09-15 03:30:42	2019-09-15 03:47:53	910	$1.5^{+0.8}_{-0.6}$	$1.5^{+1.0}_{-0.9}$	$7.5^{+20.3}_{-2.9}$			90.8/128
00010381148	58743.60379	2019-09-17 14:29:27	2019-09-17 14:45:52	1093	$0.9^{+0.5}_{-0.4}$	$0.4^{+0.7}_{-0.6}$	$2.5^{+0.5}_{-0.4}$			159.5/175
00010381149	58745.26425	2019-09-19 06:20:31	2019-09-19 06:36:51	1023	$1.4^{+0.6}_{-0.5}$	$1.3^{+0.8}_{-0.7}$	$11.6^{+2.5}_{-2.0}$			153.5/175
00010381150	58747.32460	2019-09-21 07:47:25	2019-09-21 08:01:53	1048	$1.2^{+0.7}_{-0.5}$	$1.1^{+0.9}_{-0.8}$	$4.8^{+1.2}_{-0.9}$			115.8/151
00010381151	58751.70606	2019-09-25 16:56:43	2019-09-25 17:12:54	1048	$2.1^{+0.9}_{-0.7}$	$1.6^{+0.9}_{-0.8}$	$4.2^{+0.8}_{-0.7}$			169.9/187
00010381152	58753.23374	2019-09-27 05:36:34	2019-09-27 05:50:52	958	$2.0^{+0.8}_{-0.7}$	$2.1^{+1.0}_{-0.9}$	$5.0^{+1.1}_{-0.9}$			113.7/172
00010381153	58755.35575	2019-09-29 08:32:17	2019-09-29 08:50:52	948	$1.4^{+0.7}_{-0.5}$	$1.3^{+0.9}_{-0.8}$	$6.8^{+1.5}_{-1.2}$			145.3/173
00010381154	58763.32481	2019-10-07 07:47:43	2019-10-07 08:02:53							
00010381155	58765.18065	2019-10-09 04:19:46	2019-10-09 04:35:51							
00010381156	58767.36462	2019-10-11 08:45:03	2019-10-11 09:00:53							
00010381157	58769.49017	2019-10-13 11:45:50	2019-10-13 12:02:53							
00010381158	58771.15377	2019-10-15 03:41:25	2019-10-15 03:58:53							
00010381159	58773.00434	2019-10-17 00:06:14	2019-10-17 21:15:53							
00010381160	58775.27495	2019-10-19 06:35:55	2019-10-19 06:51:53							
00010381161	58777.33271	2019-10-21 07:59:06	2019-10-21 08:14:54							

of strongly magnetized NSs in these systems and support the idea that they can be formed through the accretion induced collapse of a white dwarfs (a yet relatively poorly known NS formation channel, see Sect. 1). Furthermore, we reported on our long-term monitoring campaign on the latest discovered SyXB, IGR J17329–2731, carried out with the *Swift*/XRT up to nine months following the first detection of the source in the X-ray domain.

In the case of Sct X–1, we exploited our simultaneous *Chandra* and *NuSTAR* observation performed in 2020. The source turned out

to be relatively faint, with an average flux that decreased about two orders of magnitude compared to the previous X-ray observations carried out in 2004 with *XMM-Newton*. The slowly decreasing trend in the source flux is confirmed also by two *Suzaku* observations performed in 2014 where the source was not detected (the upper limit we provided is a factor of few higher than the flux values determined by both *Chandra* and *NuSTAR*). Although the statistics of the combined *Chandra* and *NuSTAR* data was relatively poor, we could show that the source dimming over the past decades is accompa-

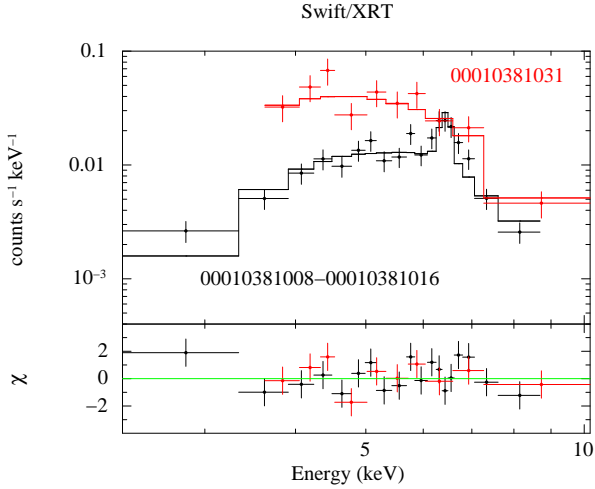


Figure 6. Unfolded spectra of IGR J17329–2731 extracted from the XRT observation 00010381031 (red), during which the source displayed a flux close to the average value, and from the combined observations 00010381008–00010381016 (black), during which the source was in one of the faint states that characterize the intra-flare emission around 58200 MJD (see Table 1). Both spectra could be described by an absorbed powerlaw, but the spectrum in the faint state clearly features a prominent iron line with a centroid energy of ~ 6.4 keV (see text for details).

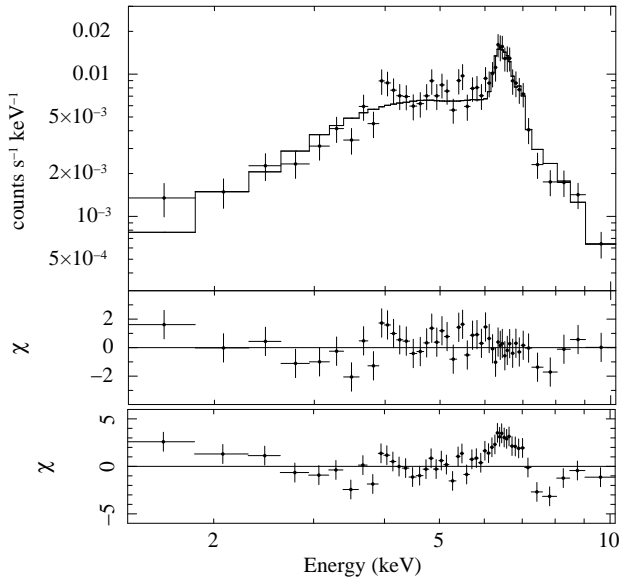


Figure 7. Merged XRT spectrum of IGR J17329–2731 obtained by combining together all observations where a iron line could be significantly detected (see Fig. 5 and Table 1). The best fit model is obtained with an absorbed power-law model and two Gaussian features at roughly 6.4 keV and 6.7 keV. The middle panel shows the residuals from the best fit when also the additional Gaussian line at roughly 6.9 keV is included, while the bottom panel shows the residuals from the best fit when all Gaussian components are removed.

nied by a moderate softening of the spectrum (the power-law photon index increased from ~ 1.5 in 2004 to roughly ~ 3.0 in 2020). No evidence of CRSF was found in the broad-band spectrum of the source. The slow decade-long dimming and softening of the source emission is not easy to interpret in the context of wind-fed SyXBs, but it is worth noticing that such behavior (accompanied by a local

absorption column density constantly in excess of 10^{23} cm^{-2}) was already reported for the other (yet poorly known) SyXB XTEJ1743–363 (Smith et al. 2012; Bozzo et al. 2013).

For 4U 1700+24, we looked for the possible presence of CRSFs in the X-ray spectral energy distribution of the source by exploiting a public (but not yet published) *NuSTAR* observation of the source, as well as simultaneous XRT+BAT spectra collected during three outbursts of the source caught by *Swift* in 2014 and 2015. When the broad-band spectrum obtained from both the FPMA and FPMB on-board *NuSTAR* is fit with a simple cut-off power-law model, significant residuals are found especially around 15 keV. These residuals suggested the presence of a broad absorption feature, similarly to what is usually expected for a CRSF. Interestingly, the FPMA and FPMB spectra also showed some marginal evidence for the first harmonic of this feature due to additional residuals around 30 keV. If our interpretation is correct, the NS hosted in 4U 1700+24 could be endowed with a magnetic field strength of $\sim 1.4 \times 10^{12}$ G (see, e.g. Staubert et al. 2019, for the conversion of the CRSF centroid energy line into the NS magnetic field strength). This is the first claim of a CRSFs in the X-ray spectrum of 4U 1700+24. We note that past investigations on the X-ray broad-band spectral energy distribution of the source were carried out (to the best of our knowledge) only by Masetti et al. (2002) and Nagae et al. (2008). These authors exploited mainly *BeppoSAX*, and *Suzaku* data where the energy range 10–30 keV is poorly covered (or missing) due to the limited overlap of the operational energies of the available instruments. Masetti et al. (2002) also reported on a *RXTE/PCA* spectrum of the source extending continuously from 3 to 20 keV. Also in this case, no CRSF was reported. We remark, however, that the fundamental line identified in our *NuSTAR* spectra would sit right at the rim of the PCA energy coverage of that spectrum and thus might have easily gone undetected in the fit. There is also the possibility that the CRSF was not visible during the PCA observation, as we know that CRSF might be dependent on the viewing direction of the observer compared to the magnetic field orientation and could change along the pulse period or at different luminosity levels (impacting, e.g., the shape of the accretion column where the CRSFs are most likely originating; see, e.g., Kretschmar et al. 2019, and references therein).

However, it must be remarked that the present statistics of the *NuSTAR* data does not allow us to firmly exclude alternative models to describe the broad-band spectral energy distribution of 4U 1700+24. The FPM spectra could be equivalently well described using the addition of a black-body component to the cut-off power-law in place of the two absorption features. The presence of a similar thermal component would not be unexpected, as it was previously reported for this source by Nucita et al. (2014) while analyzing *XMM-Newton* and *Swift*XRT data outside the outbursts. If we compare the results from these authors with those in Table 3, we note that the black-body component required by the *NuSTAR* data is significantly hotter (1.4 keV vs. the previously reported 0.7–1.0 keV) and would be dominating a large portion of the XRT energy coverage. Curiously enough, the broad-band XRT+BAT spectra that we obtained by analyzing the source behavior during three different outbursts did not show the presence of any thermal component. Although the energy coverage and statistics of all XRT+BAT data did not allow us to investigate in details the presence of the CRSF at ~ 16 keV and its harmonic, we discussed in Sect. 3 that the broad-band fits would be compatible with the (undetected) presence of these features, if their parameters are frozen to those measured by *NuSTAR*.

We thus conclude that at present it is not possible to firmly confirm

or reject the presence of CRSFs in the broad-band X-ray spectrum of 4U 1700+24. Deeper observations of this system with *NuSTAR*, featuring the uniquely required combination of sensitivity and large energy coverage, are needed to understand if 4U 1700+24 is the second SyXB to host a strongly magnetized NS and evaluate further the impact of these results for the formation channels of extreme compact objects from accreting aged white dwarfs.

IGR J17329–2731 was the first SyXB with a detected CRSF, leading to the identification in this system of a young NS endowed with a magnetic field strength of $\sim 2 \times 10^{12}$ G (see Sect 1). The observations collected during our long-term XRT monitoring showed that the source never turned off as an X-ray emitter after its initial detection and remained active at a virtually constant average flux level of few times 10^{-11} erg s $^{-1}$ cm $^{-2}$. It also underwent sporadic flares lasting a few days at the most and achieving a total dynamic range in the X-ray flux of about ~ 30 (see Fig. 5 and Table 1).

On one hand, the findings of the monitoring program corroborated the idea proposed by Bozzo et al. (2018) that IGR J17329–2731 turned on in 2017 for the first time as a SyXB, beginning effectively to be a variable but persistent source as all other objects in this class. On the other hand, the reason for the onset of such X-ray activity remains unclear. Bozzo et al. (2018) proposed that the red giant might have gone through some thermal pulse phase that had enhanced the mass loss rate toward the NS and so triggered a sufficiently intense accretion to be detectable for the first time in X-rays (explaining also the brightening of the optical star in the R-band). We can investigate here a slightly different possibility.

The flares and in general the prominent X-ray variability of the source revealed by our monitoring is commonly observed in SyXBs and usually ascribed to the presence of structures in the wind of the red giant companion (see, e.g., Yungelson et al. 2019, and references therein). It is well known that the slow ($v_{\text{wind}} \sim 10$ km s $^{-1}$) dusty winds of cool evolved stars are strongly inhomogeneous and contain large scale structures such as clumps and shells (for a recent review see Decin 2021). The structures have been directly resolved in the atmospheres of some nearby M-type giants using imaging and interferometric observations. Adam & Ohnaka (2019) show that the clumpy dusty clouds are present already within a few stellar radii in the wind of IK Tau, while the asymmetric dust emission extends to outer wind regions. The clumpy structures have typical density enhancements of a factor of ~ 3 compared to the surrounding wind. Adam & Ohnaka (2019) measured the extent of two huge clumps which have a size of ≈ 80 mas. At the distance 260 pc to the star, the measured clump size corresponds to $\approx 10^9$ km. Assuming a typical orbital velocity of 10 km s $^{-1}$ for a NS around a red giant with a period of several years, it would take the compact object about 1 yr to cross a similarly extended structure. It is thus possible that the enhancement in the mass accretion rate that was needed by IGR J17329–2731 to finally turn on as a SyXB has been caused by the NS interaction with one (or more) large stellar wind clump. If the orbit of the system is as large (or larger) than that measured for 4U 1700+24 (Hinkle et al. 2019), then we might conclude that in the past the NS has never being in contact with similarly large structures and thus no X-ray emission could ever be detected before 2017. According to this scenario, it is possible that IGR J17329–2731 will stop shining in X-rays over the time scale of one to few years, as soon as the orbit of the compact object does no longer intersect a massive stellar wind clump.

The XRT monitoring of IGR J17329–2731 also revealed the presence of intriguing obscuration events, lasting a few days (see Fig. 6 and 7). The spectral properties observed during these events are remarkably similar to those commonly recorded during X-ray

eclipses. However, it is unlikely that the NS in IGR J17329–2731 was eclipsed by its giant companion during the XRT observations. The main argument against this possibility is that the obscuration events revealed by XRT have different durations and they repeat irregularly for 5 times in less than ~ 100 days (to be compared to the typical orbital period of SyXBs of the order of years). A more likely possibility, already explored in the case of supergiant X-ray binaries where the NS is accreting from the clumpy wind of its massive companion, is that the NS in IGR J17329–2731 was temporarily obscured by a stellar wind structure located along the line of sight to the observer (see, e.g., Bozzo et al. 2011; Martínez-Núñez et al. 2017, and references therein). As we considered above that a single massive clump could be at the origin of the onset of the X-ray activity from IGR J17329–2731, we can assume that the obscuration events are most likely triggered by the presence of sub-structures within the large clump or in the surroundings. There are indications, indeed, that atmospheric structures of red giants could change on the time scale of weeks as confirmed by both observations and hydrodynamic models (see Höfner & Freytag 2019, and references therein). Furthermore, their stellar winds are permeated by shock fronts which are induced by stellar pulsations and/or convection (see, e.g., Perrin et al. 2020). The presence of a NS embedded in the wind further perturbs the atmospheric morphology with its orbital motion as well as with the effect of wind ionization by the X-ray radiation (see, e.g., Bozzo et al. 2021, and references therein). We can thus envision the possibility of the smaller scale structures being present in the wind or within the clump to induce the temporary obscuration events, as well as the short flares observed by XRT. The detection of emission lines corresponding to (at least) He-like and H-like iron further supports this scenario as the ionization of the stellar wind material is most likely occurring in the vicinity of the NS due to the X-ray radiation.

DATA AVAILABILITY

The data underlying this article are publicly available from the *XMM-Newton*, *NuSTAR*, *Chandra*, and *Swift* archives and processed with publicly available software.

ACKNOWLEDGEMENTS

We thank the anonymous referee for swift comments that helped us improve the paper. The *Swift* data of our monitoring campaigns on IGR J17329–2731 were obtained through contract ASI-INAF I/004/11/5 (PI P. Romano). PR acknowledges financial contribution from contract ASI-INAF ASI-INAF I/037/12/0. This work made use of data supplied by the UK Swift Science Data Centre at the University of Leicester (see Evans et al. 2007, 2009).

REFERENCES

- Adam C., Ohnaka K., 2019, *A&A*, **628**, A132
 Arnason R. M., Papei H., Barmby P., Bahramian A., Gorski M. D., 2021, *MNRAS*, **502**, 5455
 Bahramian A., Strader J., Heinke C. O., Sivakoff G. R., Kennea J. A., Degeenaar N., Wijnands R., 2017, *The Astronomer’s Telegram*, **10685**, 1
 Bozzo E., Falanga M., Stella L., 2008, *ApJ*, **683**, 1031
 Bozzo E., Stella L., Israel G., Falanga M., Campana S., 2009, in J. Rodriguez & P. Ferrando ed., *American Institute of Physics Conference Series Vol. 1126*, American Institute of Physics Conference Series. pp 319–321 ([arXiv:0901.3826](https://arxiv.org/abs/0901.3826)), doi:10.1063/1.3149442

- Bozzo E., et al., 2011, *A&A*, **531**, A130
- Bozzo E., Pavan L., Ferrigno C., Falanga M., Campana S., Paltani S., Stella L., Walter R., 2012, *A&A*, **544**, A118
- Bozzo E., Romano P., Ferrigno C., Esposito P., Mangano V., 2013, *Advances in Space Research*, **51**, 1593
- Bozzo E., et al., 2018, *A&A*, **613**, A22
- Bozzo E., Ducci L., Falanga M., 2021, *MNRAS*, **501**, 2403
- Bozzo E., Ferrigno C., Oskinova L., Ducci L., 2022, *MNRAS*, **510**, 4645
- Burrows D. N., et al., 2014, GRB Coordinates Network, **16829**, 1
- Burrows D. N., Chester M. M., Gehrels N., Gropp M. E., Lien A. Y., Marshall F. E., Palmer D. M., Siegel M. H., 2015, GRB Coordinates Network, **17280**, 1
- Cooke B. A., Levine A. M., Lang F. L., Primini F. A., Lewin W. H. G., 1984, *ApJ*, **285**, 258
- Corbet R. H. D., Sokoloski J. L., Mukai K., Markwardt C. B., Tueller J., 2008, *ApJ*, **675**, 1424
- De K., et al., 2022, arXiv e-prints, p. arXiv:2201.09906
- Decin L., 2021, *ARA&A*, **59**, 337
- Di Salvo T., Sanna A., 2020, arXiv e-prints, p. arXiv:2010.09005
- Evans P. A., et al., 2007, *A&A*, **469**, 379
- Evans P. A., et al., 2009, *MNRAS*, **397**, 1177
- Ferrigno C., Bozzo E., Romano P., 2020, *A&A*, **642**, A73
- Fukushima K., et al., 2014, The Astronomer's Telegram, **6850**, 1
- Fürst F., et al., 2011, *A&A*, **535**, A9
- García M., et al., 1983, *ApJ*, **267**, 291
- Heindl W. A., Rothschild R. E., Coburn W., Staubert R., Wilms J., Kreykenbohm I., Kretschmar P., 2004, in Kaaret P., Lamb F. K., Swank J. H., eds, American Institute of Physics Conference Series Vol. 714, X-ray Timing 2003: Rossi and Beyond. pp 323–330 (arXiv:astro-ph/0403197), doi:10.1063/1.1781049
- Hill R., Burginyon G., Grader R., Toor A., Stoering J., Seward F., 1974, *ApJ*, **189**, L69
- Hinkle K. H., Fekel F. C., Joyce R. R., Mikołajewska J., Gałan C., Lebzelter T., 2019, *ApJ*, **872**, 43
- Hinkle K. H., Lebzelter T., Fekel F. C., Straniero O., Joyce R. R., Prato L., Karnath N., Habel N., 2020, *ApJ*, **904**, 143
- Höfner S., Freytag B., 2019, *A&A*, **623**, A158
- Kaastra J. S., Bleeker J. A. M., 2016, *A&A*, **587**, A151
- Kaplan D. L., Levine A. M., Chakrabarty D., Morgan E. H., Erb D. K., Gaensler B. M., Moon D.-S., Cameron P. B., 2007, *ApJ*, **661**, 437
- Kennea J. A., Krimm H. A., Marshall F. E., Page K. L., Palmer D. M., Sakamoto T., Siegel M. H., 2014, GRB Coordinates Network, **17173**, 1
- Koyama K., Kunieda H., Takeuchi Y., Tawara Y., 1991a, *ApJ*, **370**, L77
- Koyama K., Kunieda H., Takeuchi Y., Tawara Y., 1991b, *ApJ*, **370**, L77
- Kretschmar P., et al., 2019, *New Astron. Rev.*, **86**, 101546
- Krimm H. A., et al., 2013, *ApJS*, **209**, 14
- Kuranov A. G., Postnov K. A., 2015, *Astronomy Letters*, **41**, 114
- Liu J., Soria R., Qiao E., Liu J., 2018, *MNRAS*, **480**, 4746
- Lü G.-L., Zhu C.-H., Postnov K. A., Yungelson L. R., Kuranov A. G., Wang N., 2012, *MNRAS*, **424**, 2265
- Martínez-Núñez S., et al., 2017, *Space Sci. Rev.*, **212**, 59
- Masetti N., et al., 2002, *A&A*, **382**, 104
- Masetti N., Orlandini M., Palazzi E., Amati L., Frontera F., 2006, *A&A*, **453**, 295
- Masetti N., Rigon E., Maiorano E., Cusumano G., Palazzi E., Orlandini M., Amati L., Frontera F., 2007a, *A&A*, **464**, 277
- Masetti N., et al., 2007b, *A&A*, **470**, 331
- Nagae O., Takahashi H., Shirai H., Fukazawa Y., 2008, in Microquasars and Beyond. p. 102
- Nespoli E., Fabregat J., Mennickent R. E., 2008, *A&A*, **486**, 911
- Nucita A. A., Carpano S., Guainazzi M., 2007, *A&A*, **474**, L1
- Nucita A. A., Stefanelli S., De Paolis F., Masetti N., Ingrassio G., Del Santo M., Manni L., 2014, *A&A*, **562**, A55
- Perrin G., et al., 2020, *A&A*, **642**, A82
- Postel A., Kuulkers E., Savchenko V., Sanchez-Fernandez C., Wijnands R., Pottschmidt K., Beckmann V., Bozzo E., 2017, The Astronomer's Telegram, **10644**
- Postnov K., et al., 2010, in Eighth Integral Workshop. The Restless Gamma-ray Universe (INTEGRAL 2010). p. 15 (arXiv:1110.1156)
- Schönherr G., Wilms J., Kretschmar P., Kreykenbohm I., Santangelo A., Rothschild R. E., Coburn W., Staubert R., 2007, *A&A*, **472**, 353
- Shakura N., Postnov K., Kochetkova A., Hjalmarsdotter L., 2012, *MNRAS*, **420**, 216
- Smith D. M., Markwardt C. B., Swank J. H., Negueruela I., 2012, *MNRAS*, **422**, 2661
- Staubert R., et al., 2019, *A&A*, **622**, A61
- Tauris T. M., 2015, arXiv e-prints, p. arXiv:1501.03882
- Torrejón J. M., Schulz N. S., Nowak M. A., Kallman T. R., 2010, *ApJ*, **715**, 947
- Truemper J., Pietsch W., Reppin C., Voges W., Staubert R., Kendziorra E., 1978, *ApJ*, **219**, L105
- Trümper J., Pietsch W., Reppin C., Sacco B., 1977, in Papagiannis M. D., ed., Vol. 302, Eighth Texas Symposium on Relativistic Astrophysics. p. 538, doi:10.1111/j.1749-6632.1977.tb37072.x
- Verner D. A., Yakovlev D. G., 1995, *A&AS*, **109**, 125
- Verner D. A., Ferland G. J., Korista K. T., Yakovlev D. G., 1996, *ApJ*, **465**, 487
- Wang Y.-M., 1981, *A&A*, **102**, 36
- Wilms J., Allen A., McCray R., 2000, *ApJ*, **542**, 914
- Yungelson L. R., Kuranov A. G., Postnov K. A., 2019, *MNRAS*, **485**, 851